

HYDROGEN PHASES ON THE SURFACE OF A STRONGLY MAGNETIZED NEUTRON STAR

Dong Lai

*Theoretical Astrophysics, 130-33, California Institute of Technology
Pasadena, CA 91125*

E-mail: dong@tapir.caltech.edu

Edwin E. Salpeter

*Center for Radiophysics and Space Research, Cornell University
Ithaca, NY 14853*

(March 1997)

ABSTRACT

The outermost layers of some neutron stars are likely to be dominated by hydrogen, as a result of fast gravitational settling of heavier elements. These layers directly mediate thermal radiation from the stars, and determine the characteristics of X-ray/EUV spectra. For a neutron star with surface temperature $T \lesssim 10^6$ K and magnetic field $B \gtrsim 10^{12}$ G, various forms of hydrogen can be present in the envelope, including atom, poly-molecules, and condensed metal. We study the physical properties of different hydrogen phases on the surface of a strongly magnetized neutron star for a wide range of field strength B and surface temperature T . Depending on the values of B and T , the outer envelope can be either in a nondegenerate gaseous phase or in a degenerate metallic phase. For $T \gtrsim 10^5$ K and moderately strong magnetic field, $B \lesssim 10^{13}$ G, the envelope is nondegenerate and the surface material gradually transforms into a degenerate Coulomb plasma as density increases. For higher field strength, $B \gg 10^{13}$ G, there exists a first-order phase transition from the nondegenerate gaseous phase to the condensed metallic phase. The column density of saturated vapor above the metallic hydrogen decreases rapidly as the magnetic field increases or/and temperature decreases. Thus the thermal radiation can directly emerge from the degenerate metallic hydrogen surface. The characteristics of surface X-ray/EUV emission for different phases are discussed. A separate study concerning the possibility of magnetic field induced nuclear fusion of hydrogen on the neutron star surface is also presented.

Subject headings: stars: neutron – stars: atmospheres – magnetic fields – atomic processes – equation of state – radiation mechanisms: thermal

1. INTRODUCTION

It has long been realized that neutron stars should remain detectable as soft X-ray sources for $\sim 10^5$ years after their birth (Chiu & Salpeter 1964; Tsuruta 1964). The last thirty years have seen significant progress in our understanding of various physical processes responsible to neutron star cooling (see e.g., Pethick 1992; Umeda, Tsuruta & Nomoto 1994; Reisenegger 1995). The advent of imaging X-ray telescopes has now made it possible to observe isolated neutron stars directly by their surface radiation. In particular, ROSAT has detected pulsed X-ray thermal emission from a number of radio pulsars (see Becker 1995 for a review). Several nearby pulsars have also been detected by EUVE (Edelstein & Bowyer 1996). On the other hand, old isolated neutron stars ($10^8 - 10^9$ of which are thought to exist in the Galaxy), heated through accretion from interstellar material, are also expected to be common sources of soft X-ray/EUV emission (e.g, Treves & Colpi 1991; Blaes & Madau 1993. See Walter et al. 1996 for a possible detection and Pavlov et al. 1996 for spectral interpretations). It has been suggested that some of the unidentified sources detected in the EUVE and ROASAT WFC all-sky surveys may be associated with such old neutron stars (Shemi 1995). Overall, the detections of the surface emission from neutron stars have the potential of constraining the nuclear equation of state, various heating/accretion processes, magnetic field structure and surface chemical composition. Future observations are likely to extend to surface temperatures as low as 10^5 K. Confrontation with theory requires detailed understanding of the physical properties of the outer layers of neutron stars, in the presence of intense magnetic fields ($B \gtrsim 10^{12}$ G) and low temperatures.

For young radio pulsars that have not accreted much gas, one might expect the surfaces to consist mainly of iron-peak elements formed at the neutron star birth. However, once the neutron stars accrete material, or have gone through a phase of accretion, either from the interstellar medium or from a binary companion, a hydrogen envelope will form on the top of the surface unless it is completely burnt out. It is this envelope that mediates the radiation from the neutron star surface. While the strong magnetic field and/or rapid stellar spin may prevent large-scale accretion, it should be noted that even with a low accretion rate of 10^{10} g s $^{-1}$ (typical of accretion from the interstellar medium) for one year, the accreted material will be more than enough to completely shield the iron surface of a neutron star. The lightest elements, H and He, are likely to be the most important chemical species in the envelope due to their predominance in the accreting gas and also due to quick separation of light and heavy elements in the gravitational field of the neutron star (e.g., the settling time of C in a 10^6 K hydrogen photosphere is of order a second). If the present accretion rate is low, gravitational settling produces a pure H atmosphere. If the temperature on the neutron star surface is not too high, light atoms, molecules and metal grains may form. The purpose of this paper is to study the phase diagram and the physical properties of the hydrogen envelope for a wide range of magnetic field strength and surface temperature.

A strong magnetic field can dramatically change the structure of atoms, molecules and condensed matter (see Ruderman 1974 for an early review, and Ruder et al. 1994 for a recent text. Heavier atoms are also discussed by Lieb et al. 1994). The atomic unit B_o for the magnetic field strength and a dimensionless parameter b are

$$b \equiv \frac{B}{B_o}; \quad B_o = \frac{m_e^2 e^3 c}{\hbar^3} = 2.351 \times 10^9 \text{ G}. \quad (1.1)$$

When $b \gg 1$, the cyclotron energy of the electron $\hbar\omega_e = \hbar(eB/m_e c) = 11.58 B_{12}$ keV, where $B_{12} = b/425.4$ is the magnetic field strength in units of 10^{12} G, is much larger than the typical

Coulomb energy, thus the Coulomb forces act as a perturbation to the magnetic forces on the electrons, and at most temperatures the electrons settle into the ground Landau level. Because of the extreme confinement of electrons in the transverse direction, the Coulomb force becomes much more effective for binding electrons in the parallel direction. The atom has a cigar-like structure. Moreover, it is possible for these elongated atoms to form molecular chains by covalent bonding along the field direction. In two recent papers (Lai, Salpeter & Shapiro 1992; Lai & Salpeter 1996; hereafter referred as Paper I and Paper II), we have studied the electronic structure and energy levels of various forms of hydrogen in strong magnetic field, including atoms, poly-molecular chains H_N and condensed metal. In contrast to Fe chains, which is unbound at zero-pressure (Jones 1985; Neuhauser, Koonin & Langanke 1987), we found that for typical magnetic field strength, $B_{12} \gtrsim 1$, the infinite H chains (thus the metallic hydrogen) are bound relative to individual atoms, and the cohesive energy increases with the field strength. This gives rise to the possibility of condensation of metallic hydrogen for sufficiently low temperature and/or high magnetic field. We quantify this phase transition in §4 of this paper.

In this study, we shall focus on the magnetic field strength in the range of $10^{11} \lesssim B \lesssim 10^{15}$ G so that $b \gg 1$ is well-satisfied. While field strengths of order $10^{12} - 10^{13}$ G are considered typical for most neutron stars (with the exception of old millisecond pulsars and neutron stars in low-mass X-ray binaries), it should be noted that the only physical upper limit to the neutron star magnetic field strength is the virial equilibrium value, $\sim 10^{18}$ G. Indeed, it has been suggested that magnetic fields as strong as 10^{15} G may be easily generated by dynamo processes in nascent neutron stars (Thompson & Duncan 1993), and may be required for soft gamma-ray repeaters (Paczynski 1992; Duncan & Thompson 1993).

Following the pioneering study of non-magnetic neutron star atmospheres by Romani (1987), recent atmosphere modeling has taken account of the transport of different photon modes through an ionized medium in strong magnetic field (Pavlov et al. 1994, 1995; Zavlin et al. 1995). Neutral atoms have been studied in detail for zero-field atmospheres (Rajagopal & Romani 1996; Zavlin et al. 1996). Magnetic atoms have also been included in some models (Miller 1992), although many problems related to the treatment of the bound states in a strong magnetic field still remain. One outstanding issue concerns the non-trivial coupling between the center-of-mass motion and internal structure of the atom (e.g., Avron, Herbst & Simon 1978; Herold, Ruder & Wunner 1981). This has been considered in detail in our recent paper (Lai & Salpeter 1995; hereafter Paper III) and used to derive the generalized Saha equation for ionization-recombination equilibrium. With this, we are now in a good position to calculate reliable composition and construct the complete phase diagram of the magnetic hydrogen surface of a neutron star. The published atmosphere models have shown that neutral hydrogen is important for zero-field, cool atmospheres ($T \sim 10^5$ K), but we shall see that even at $B_{12} \sim 0.01$ its importance extends to higher temperatures. Moreover, we shall find that at high field strength polyatomic molecules (for $B_{12} \gtrsim 1$) and even the condensed phase (for $B_{12} \gtrsim 100$) are important.

Our paper is organized as follows. In §2 we discuss the physics of various hydrogen bound states in a strong magnetic field. In §3 we study the physical properties of the nondegenerate atmosphere, including the abundance of various species. We consider the phase equilibrium of the metallic state in §4. Some astrophysical implications of our results are discussed in §5. Appendix B includes a study of the magnetic field induced pycnonuclear reactions that occur on neutron star surfaces.

Throughout the paper we shall use real physical units and atomic units (a.u.) interchangeably, whichever is more convenient. Recall that in atomic units, mass and length

are expressed in units of the electron mass m_e and the Bohr radius $a_o = 0.529 \times 10^{-8}$ cm, energy in units of 2 Rydberg $= e^2/a_o = 2 \times 13.6$ eV; field strength in units of B_o (Eq. [1.1]), temperature in units of 3.15×10^5 K, and pressure in units of $e^2/a_o^4 = 2.94 \times 10^{14}$ dynes cm^{-2} .

2. HYDROGEN BOUND STATES IN STRONG MAGNETIC FIELD

Here we briefly review the physics of various forms of hydrogen bound states in a strong magnetic field. The detailed quantum mechanical calculations are described in Paper I and Paper II, where extensive references can be found. Our main results are summarized in various fitting formulae for the binding energies and in Table 1.

Our discussions are based on nonrelativistic quantum mechanics, even for extremely high magnetic field, $B \gtrsim B_{\text{rel}} = (\hbar c/e^2)^2 B_o = 4.414 \times 10^{13}$ G, at which the transverse motion of the electron becomes relativistic. This nonrelativistic treatment of bound states is valid because (i) the electron remains nonrelativistic in the z -direction (along the field axis) as long as the binding energy is much less than $m_e c^2$, and (ii) the shape of the Landau wavefunction in the relativistic theory is the same as in the nonrelativistic theory, as the cyclotron radius

$$\hat{\rho} = \left(\frac{\hbar c}{eB} \right)^{1/2} = \frac{1}{b^{1/2}} \text{ (a.u.)} = 2.57 \times 10^{-10} B_{12}^{-1/2} \text{ (cm)},$$

is independent of the particle mass. Thus our results should be reliable even for the highest field strength considered in this paper. In §2.3, we shall include a discussion of the density-induced relativistic effect when we consider the metallic hydrogen state.

2.1 Atoms

In a superstrong magnetic field satisfying $b \gg 1$, the spectra of the H atom can be specified by two quantum numbers (m, ν) , where $m = 0, 1, 2, \dots$ measures the mean separation $\rho_m = (2m+1)^{1/2} \hat{\rho}$ of the electron and proton in the transverse direction (perpendicular to the field), while ν is the number of nodes of the electron's z -wavefunction (along the field axis). The states with $\nu \neq 0$ resemble the zero-field hydrogen atom with small binding energy $|E_\nu| \simeq 1/(2\nu^2)$ and we shall mostly focus on the tightly-bound states with $\nu = 0$. For the ground state $(0, 0)$, the sizes (in atomic units) of the atomic wavefunction perpendicular and parallel to the field are of order $L_\perp \sim \hat{\rho} = b^{-1/2}$ and $L_z \sim l^{-1}$, where $l \equiv \ln b$. The binding energy $|E(\text{H})|$ (or the ionization energy Q_1) of the atom is given by

$$Q_1 = |E(\text{H})| \simeq 0.16 l^2 \text{ (a.u.)} \simeq 161 \left[\frac{\ln(426 B_{12})}{\ln 426} \right]^2 \text{ (eV)}. \quad (2.1)$$

The numerical factor 0.16 in equation (2.1) is an approximate value for $B_{12} \gtrsim 1$ (More accurate fitting can be found in Paper II). Some numerical values are given in Table 1. The tightly-bound excited states $(m, 0)$ have the transverse size $L_\perp \sim \rho_m = [(2m+1)/b]^{1/2}$. For $2m+1 \ll b$, we have $L_z \sim 1/\ln(1/\rho_m)$, and

$$E_m \simeq -0.16 l_m^2 = -0.16 \left(\ln \frac{b}{2m+1} \right)^2 \text{ (a.u.)} \quad (\text{for } 2m+1 \ll b). \quad (2.2a)$$

For $2m + 1 \gtrsim b$, we have $L_z \sim \rho_m^{1/2}$, and the energy levels are approximated by

$$E_m \simeq -0.6 \left(\frac{b}{2m + 1} \right)^{1/2} \quad (\text{a.u.}) \quad (\text{for } 2m + 1 \gtrsim b). \quad (2.2b)$$

Note that, unlike the field-free case, the excitation energy $\Delta E_m = |E(\text{H})| - |E_m|$ is small compared with $|E(\text{H})|$.

The above results assume a fixed Coulomb potential produced by the proton (i.e., infinite proton mass). The use of a reduced electron mass $m_e m_p / (m_e + m_p)$ only introduces a very small correction to the energy (of order m_e / m_p). However, as mentioned in §1, the effect of the center-of-mass motion on the energy spectra is rather subtle in strong magnetic field. We will come back to this point in Sec. 3.2 (see Paper III).

2.2 Molecules

In a superstrong magnetic field, the mechanism of forming molecules is quite different from the zero-field case (Ruderman 1974; Papers I-II). The spins of the electrons of the atoms are all aligned anti-parallel to the magnetic field, and therefore two atoms in their ground states ($m = 0$) do not easily bind together according to the exclusion principle. Instead, one H atom has to be excited to the $m = 1$ state. The two H atoms, one in the ground state ($m = 0$), another in the $m = 1$ state then form the ground state of the H_2 molecule by covalent bonding. Since the “activation energy” for exciting an electron in the H atom from Landau orbital m to $(m + 1)$ is small (see Eq. [2.2]), the resulting molecule is stable. In this way, more atoms can be added to form a larger molecule, in contrast to the field-free case.

For a given magnetic field, as the number of H atoms N increases, the electrons occupy more and more Landau orbits (with $m = 0, 1, 2, \dots, N - 1$), but the length of the chain decreases so that the volume per electron of the electron distribution is of order (neglecting logarithmic factors) $(bN)^{-1}$. Beyond some critical number $N_s \sim (b/l^2)^{1/5}$, it becomes energetically more favorable for the electrons to settle into the inner Landau orbitals (with smaller m) with nodes in their longitudinal wavefunctions (i.e., $\nu \neq 0$). For $N \gtrsim N_s$, the energy per atom in the H_N molecule, $|E(\text{H}_N)|/N$, asymptotes to a value $\sim b^{2/5}$, independent of N , and the volume per electron to $\sim b^{-6/5}$ (Paper I; see §2.3). For a typical magnetic field strength of interest here, the energy saturation point is $N_s \sim 3 - 5$.

The dimensions of the H_2 molecule parallel and perpendicular to the magnetic field are comparable to those of the atom. The binding energies also approximately scale as $(\ln b)^2$, but they are numerically smaller than the ionization energy of H atom. More precisely, the *dissociation energy* of H_2 can be fitted by

$$Q_2^{(\infty)} \equiv 2|E(\text{H})| - |E(\text{H}_2)| = 0.106 [1 + \tau \ln(b/b_{\text{crit}})] l^2 \quad (\text{a.u.}), \quad \tau \simeq 0.1 l^{0.2}, \quad (2.3)$$

with an accuracy of $\lesssim 5\%$ for $1 \lesssim B_{12} \lesssim 1000$, where $b_{\text{crit}} = 1.80 \times 10^4$ is to be defined in equation (3.8) (The superscript “ (∞) ” implies that the zero-point energy of the molecule is not included in $Q_2^{(\infty)}$; see §2.4). Thus $Q_2^{(\infty)} \simeq 46$ eV for $B_{12} = 1$ and $Q_2^{(\infty)} \simeq 150$ eV for $B_{12} = 10$ (cf. Table 1). By contrast, the zero-field dissociation energy of H_2 is 4.75 eV.

For the ground state of H_2 , the molecular axis and the magnetic field axis coincide, and the two electrons occupy the $m = 0$ and $m = 1$ orbitals, i.e., $(m_1, m_2) = (0, 1)$. The molecule can have different types of excitation levels (Paper II):

(i) *Electronic excitations.* The electrons occupy different orbitals other than $(m_1, m_2) = (0, 1)$, giving rise to the electronic excitations. The energy difference between the excited

state (m_1, m_2) (with $\nu_1 = \nu_2 = 0$) and the ground state $(0, 1)$ is approximately proportional to $\ln b$, as in the case for atoms. Typically, only the single-excitation levels (those with $m_1 = 0$ and $m_2 > 1$) are bound relative to two atoms in the ground states. Another type of electronic excitation is formed by two electrons in the $(m, \nu) = (0, 0)$ and $(0, 1)$ orbitals. The dissociation energy of this weakly-bound state is of order a Rydberg, and does not depend sensitively on the magnetic field strength.

(ii) *Aligned vibrational excitations.* These result from the vibration of the protons along the magnetic field axis. For the electronic ground state, the energy quanta of small-amplitude oscillations is approximately given by

$$\hbar\omega_{\parallel} \simeq 0.13 (\ln b)^{5/2} \mu^{-1/2} (\text{a.u.}) \simeq 0.12 (\ln b)^{5/2} (\text{eV}), \quad (2.4)$$

where $\mu = m_p/2m_e = 918$ is the reduced mass of the two protons in units of the electron mass. Thus $\hbar\omega_{\parallel} \simeq 10$ eV at $B_{12} = 1$ and $\hbar\omega_{\parallel} \simeq 23$ eV at $B_{12} = 10$, in contrast to the vibrational energy quanta $\hbar\omega_{\text{vib}} \simeq 0.52$ eV for H_2 molecule in zero magnetic field.

(iii) *Transverse vibrational excitations.* The molecular axis can deviate from the magnetic field direction, precesses and vibrates around the field line. Such an oscillation is the high-field analogy of the usual molecular rotation. The important difference is that here this “rotation” is constrained around the magnetic field line. For the ground electronic state, the excitation energy quanta $\hbar\omega_{\perp 0}$ is given by

$$\hbar\omega_{\perp 0} \simeq 0.125 b^{1/2} (\ln b) \mu^{-1/2} (\text{a.u.}) \simeq 0.11 b^{1/2} (\ln b) (\text{eV}), \quad (2.5)$$

where the subscript “0” indicates that we are at the moment neglecting the magnetic forces on the protons which, in the absence of the Coulomb forces, lead to the cyclotron motion of the protons (see §2.4). Thus $\hbar\omega_{\perp 0} \simeq 14$ eV at $B_{12} = 1$ and $\hbar\omega_{\perp 0} = 65$ eV at $B_{12} = 10$.

It is important to note that in strong magnetic field, the electronic and vibrational (aligned and transverse) excitations are all comparable, with $\hbar\omega_{\perp 0} \gtrsim \hbar\omega_{\parallel}$. This is in contrast to the zero-field case, where one has $\Delta\varepsilon_{\text{elec}} \gg \hbar\omega_{\text{vib}} \gg \hbar\omega_{\text{rot}}$.

2.3 Infinite Chains and the Condensed Metallic State

For $N \gg N_s$, the binding energy per atom in a H_N molecule saturates, and the structure of the molecule is the same as that of an infinite chain H_{∞} . By placing a pile of parallel infinite chains close together (with spacing of order $b^{-2/5}$ a.u.), a three-dimensional condensed metal can be formed (e.g., body-centered tetragonal lattice; Ruderman 1971). We offer our assessment on various calculations of the binding energy of magnetic Coulomb lattice.

2.3.1 Uniform Electron Gas Model and its Extension

The binding energy of the magnetic metal at zero pressure can be estimated using the uniform electron gas model (e.g., Kadomtsev 1970). Consider a Wigner-Seitz cell with radius r_s , volume $V_s = 4\pi r_s^3/3$ (the mean number density of electron is then $n_e = 1/V_s$). When the electron Fermi energy $p_F^2/(2m_e) = (n_e \hbar^2 c/2eB)^2/2m_e$ is less than the cyclotron energy $\hbar\omega_e$, or when the density satisfies

$$n_e \leq n_{\text{Landau}} = \frac{eB}{hc} \frac{2}{\hbar} (2m_e \hbar\omega_e)^{1/2} = \frac{1}{\sqrt{2}\pi^2 \hat{\rho}^3} = 0.0716 b^{3/2} (\text{a.u.}); \quad (2.6)$$

$$r_{s,\text{Landau}} = 1.49 b^{-1/2} (\text{a.u.}),$$

the electrons only occupy the ground Landau level. In the simple uniform electron gas model, the energy per cell of the metallic hydrogen can be written as

$$E_s(r_s) = \frac{3\pi^2}{8b^2r_s^6} - \frac{0.9}{r_s} \quad (\text{a.u.}), \quad (2.7)$$

where the first term is the kinetic energy $E_k = (2\pi^4/3m_e)(\hbar^2c/eB)^2n_e^2$, and the second term is the Coulomb energy. For the zero-pressure metal, we have $dE_s/dr_s = 0$, and the equilibrium r_s and energy are then given by

$$r_{s,0} \simeq 1.90 b^{-2/5} \quad (\text{a.u.}), \quad E_{s,0} \simeq -0.395 b^{2/5} \quad (\text{a.u.}). \quad (2.8)$$

The corresponding mass density is $\rho_{s,0} \simeq 560 B_{12}^{6/5} \text{ g cm}^{-3}$, which is much smaller than the Landau density, defined in Eq. (2.6), by a factor $0.48 b^{-3/10}$. The pressure P in a metal compressed to, say, twice the zero-pressure density $\rho_{s,0}$, is a few times $r_{s,0}^{-3}|E_{s,0}|$, i.e., of order $P \sim 0.1 b^{8/5} \sim 10^3 B_{12}^{8/5} \quad (\text{a.u.})$. Pressures in a neutron star surface layer of interest are much smaller than this and we need to consider only $n_e < n_{\text{Landau}}$.

We now discuss several corrections to the simple uniform electron gas model for metallic hydrogen.

(i) *Relativistic effect.* As noted before, the use of non-relativistic equations for the transverse motion of the electrons is a good approximation even for $B \gtrsim B_{\text{rel}} \simeq 137^2 B_o$. We can show that the density-induced relativistic effect is also small. The critical density n_{Landau} for onset of Landau excitation is still given by equation (2.6). The relativistic parameter is $x_e \equiv p_F/(m_e c) = (n_e/n_{\text{Landau}})(2B/B_{\text{rel}})^{1/2}$. At zero-pressure density, using equation (2.8), we have $x_e \simeq 5.03 \times 10^{-3} b^{1/5}$. Thus near zero-pressure density, the relativistic effect is always negligible for the range of field strength of interest in this paper.

(ii) *Coulomb exchange interaction.* The exclusion principle for the electron results in an exchange correction to the Coulomb energy. The Dirac exchange energy (in atomic units) per electron is given by $E_{ex} = -3F/(4br_s^3)$, where F is a function of the ratio n_e/n_{Landau} (Fushiki, Gudmundsson & Pethick 1989). The effect of this (negative) exchange interaction is to increase $r_{s,0}$ and $|E_{s,0}|$.

(iii) *Non-uniformity of the electron gas.* The Thomas-Fermi screening wavenumber k_{TF} is given by (e.g., Ashcroft & Mermin 1976) $k_{TF}^2 = 4\pi e^2 D(E_F)$, where $D(E_F) = \partial n_e / \partial E_F$ is the density of states per unit volume at the Fermi surface $E = E_F = p_F^2/(2m_e)$. Since $n_e = (2eB/\hbar^2 c)p_F$, we have $D(E_F) = n_e/2E_F = (m_e/n_e)(2eB/\hbar^2 c)^2$, and

$$k_{TF} = \left(\frac{4}{3\pi^2} \right)^{1/2} b r_s^{3/2} \quad (\text{a.u.}). \quad (2.9)$$

(More details on the electron screening in strong magnetic field, including the anisotropic effect, can be found in Horing 1969). The gas is uniform when the screening length k_{TF}^{-1} is much longer than the particle spacing r_s , i.e., $k_{TF} r_s \ll 1$. For the zero-pressure metal, using equation (2.8), we have $k_{TF} r_s \simeq 1.83$, independent of B . Thus even as $B \rightarrow \infty$, the electron non-uniformity must be considered for the zero-pressure metal. This effect can be studied using the Thomas-Fermi type statistical model, including the exchange and the Weizsäcker gradient corrections (see Fushiki et al. 1992 and references therein).

2.3.2 Cohesive Energy of the Condensed State

Although the simple uniform electron gas model and its Thomas-Fermi type extensions yield reasonable binding energy for the metallic state, their validity and accuracy in the strong

field regime cannot be easily justified, and it is the difference between the energy of the metal and that of the atom that determines whether the metal is bound. One uncertainty concerns the lattice structure of the metal, since the Madelung energy can be very different from the Wigner-Seitz value (the second term in Eq. [2.7]) for a non-cubic lattice. In principle, a three-dimensional electronic band structure calculation is needed to resolve this problem, as Jones (1985, 1986) has attempted for carbon and iron using density functional theory. However, the electron correlation has not been taken into account, and, like the Thomas-Fermi type statistical models, the accuracy of density functional approximation in a strong magnetic field is not yet known (for a review of density functional theory as applied to non-magnetic terrestrial solids, see, e.g., Callaway & March 1984).

We consider the self-consistent Hartree-Fock method (Neuhauser, Koonin & Langanke 1987; Paper I) to be the most reliable approach to the problem. This has only been done for one-dimensional chains. Our numerical results for the energy (per atom) of the H_∞ chain can be fitted (to within 2% accuracy for B_{12} up to $\sim 10^3$) to a form similar to equation (2.8):

$$E_\infty = -0.76 b^{0.37} \text{ (a.u.)} = -194 B_{12}^{0.37} \text{ (eV)}. \quad (2.10)$$

Note that $|E_\infty|$ in equation (2.10) is larger than equation (2.8) by a factor of 1.8. The cohesive energy of the 1d chain (energy release in $H+H_\infty = H_{\infty+1}$) is given (to within $\lesssim 10\%$ accuracy) by

$$Q_\infty^{(\infty)} = |E_\infty| - |E(H)| \simeq 0.76 b^{0.37} - 0.16 (\ln b)^2 \text{ (a.u.)} \quad (2.11)$$

where the superscript “ (∞) ” indicates that the zero-point energy correction to the cohesive energy has yet to be included (§2.4).

The energy difference $\Delta E_s = |E_{s,0}| - |E_\infty|$ between the 3d metal and the 1d chain must be positive and can be estimated by considering the interaction (mainly quadrupole - quadrupole) between the chains. We have found (Appendix A) that this difference is probably between 0.4% and 1% of $|E_\infty|$. Therefore, for hydrogen, *the binding of the three dimensional metal results mainly from the covalent bond along the magnetic field axis, not from the chain-chain interaction.* The cohesive energy of the zero-pressure H metal is $Q_s = Q_\infty + \Delta E_s$.

A note about the difference between iron and hydrogen is appropriate at this point. For Fe, it has been found that at $B_{12} \sim 1 - 10$, the infinite chain is not bound relative to the atom (Jones 1985; Neuhauser et al. 1987), contrary to what the original calculations (e.g., Flowers et al. 1977) indicate. Therefore, the chain-chain interaction must play a crucial role in determining whether the three dimensional zero-pressure Fe metal is bound or not. The main difference between Fe and H is that for the Fe atom at $B_{12} \sim 1$, many electrons are populated in the $\nu \neq 1$ states, whereas for the H atom, as long as $b \gg 1$, the electron always settles down in the $\nu = 0$ tightly-bound state. Therefore, the covalent bonding mechanism for forming molecules (cf. §2.2) is not effective for Fe at $B_{12} \sim 1$. However, for sufficiently high B field, when $a_o/Z \gg \sqrt{2Z+1}\hat{\rho}$, or $B_{12} \gg 100(Z/26)^3$, we expect the Fe chain to be bound in a similar fashion as the H chain discussed here.

2.4 Zero-Point Energies and Relative Binding Energies of Different Forms of Hydrogen

For the H_2 molecule, the zero-point energy of the aligned vibration is $\hbar\omega_{\parallel}/2$ (Eq. [2.4]). Equation (2.5) for the zero-point energy of the transverse oscillation includes only the contribution of the electronic restoring potential $\mu\omega_{\perp 0}^2 R_{\perp}^2/2$. Since the magnetic forces on the protons also induce a “magnetic restoring potential” $\mu\omega_p^2 R_{\perp}^2/2$, the zero-point energy of the transverse oscillation is (Paper II)

$$\hbar\omega_{\perp} = \hbar(\omega_{\perp 0}^2 + \omega_p^2)^{1/2} - \hbar\omega_p, \quad (2.12)$$

where $\hbar\omega_p = \hbar eB/(m_p c) \simeq 6.3 B_{12}$ eV is the cyclotron energy of proton. Thus dissociation of H_2 taking into account the zero-point energies is

$$Q_2 = Q_2^{(\infty)} - \left(\frac{1}{2} \hbar\omega_{\parallel} + \hbar\omega_{\perp} \right). \quad (2.13)$$

Now consider the zero-point energy in the metallic hydrogen. Neglecting the magnetic force, the zero-point energy E_{zp} of a proton in the lattice is of order $\hbar\Omega_p$, where $\Omega_p = (4\pi e^2 n_e / m_p)^{1/2}$ is the ion plasma frequency. Thus for the zero-pressure metal, we have

$$E_{zp} \sim \hbar\Omega_p = 0.040 r_s^{-3/2} \text{ (a.u.)} \simeq 0.015 b^{3/5} \text{ (a.u.)}. \quad (2.14)$$

This is much smaller than the total binding energy (Eq. [2.10]) unless $B_{12} \gtrsim 10^5$. This means that for the range of field strength considered in this paper, the zero-point amplitude is small compared to the lattice spacing. Thus quantum melting is not effective (Ceperley & Alder 1980) and the metal is a solid at zero temperature. Accurate determination of E_{zp} requires a detailed understanding of the lattice phonon spectra. At zero-field, Monte-Carlo simulations give $E_{zp} \simeq 3\hbar\Omega_p\eta/2$, with $\eta \simeq 0.5$ (Hansen & Pollock 1973). For definiteness, we will adopt the same value for E_{zp} in a strong magnetic field. Taking into account the magnetic effect on the proton, the corrected cohesive energy of 1d chain is expected to be

$$Q_{\infty} = Q_{\infty}^{(\infty)} - \left[\frac{1}{2} \hbar\Omega_p\eta + \hbar \left(\frac{\omega_p^2}{4} + \eta^2 \Omega_p^2 \right)^{1/2} - \frac{1}{2} \hbar\omega_p \right], \quad (2.15)$$

with $\eta \simeq 0.5$. As mentioned in §2.3, the relative binding energy between 3d condensate and 1d chain is close to 0.4% – 1% of $|E_{\infty}|$. We shall consider the condensed phase only for $B_{12} > 10$, where the ratio $Q_{\infty}/|E_{\infty}|$ ranges from 0.3 to 0.7 for $B_{12} = 10 - 500$. For definiteness we shall express the cohesive energy of the 3d condensate as

$$Q_s = |E_{s,0}| - |E(H)| = Q_{\infty} + \Delta E_s = (1 + \alpha)Q_{\infty}, \quad (2.16)$$

with $\alpha \simeq 0.01 - 0.02$.

To summarize, we plot in Figure 1 the energy releases Q_1 , Q_2 and Q_{∞} for $e+p=H$, $H+H=H_2$, and $H+H_{\infty} = H_{\infty+1}$ respectively. Some numerical values are given in Table 1. The zero-point energy corrections for Q_2 and Q_{∞} have been included in the figure (if they are neglected, the curves are qualitatively similar, although the exact values of the energies are somewhat changed.) Although $b \gg 1$ satisfies the nominal requirement for the “strong field” regime, a more realistic expansion parameter for the stability of the condensed state over atoms and molecules (cf. Eqs. [2.1], [2.3], [2.8] and [2.11]) is the ratio $b^{0.4}/(\ln b)^2$. This ratio exceeds 0.3, and increases rapidly with increasing field strength only for $b \gtrsim 10^4$. For $B_{12} \lesssim 10$, we see that $Q_1 > Q_2 > Q_{\infty}$ (cf. Fig. 1), the condensed metallic phase may (or may not) exist in the atmosphere. Fortunately, at the temperatures of interest in this paper we shall need to consider the condensed state only for $B_{12} \gtrsim 10$, where $Q_1 > Q_{\infty} > Q_2$ (for $10 \lesssim B_{12} \lesssim 100$) or $Q_{\infty} > Q_1 > Q_2$ (for $B_{12} \gtrsim 100$). This will have important consequences on the composition of the saturated vapor above the condensed phase (§4).

2.5 Surface Energy of Droplets and Large Molecules

For a single linear molecule H_N we write Q_N as the dissociation energy into $H_{N-1}+H$ and denote the limit for an infinite chain as Q_{∞} . Numerical values and fitting formulae for

TABLE 1
Relative Binding Energies (in eV) of H, H₂ and H_∞

B_{12}	Q_1	$Q_2^{(\infty)}$	Q_2	$Q_\infty^{(\infty)}$	Q_∞
0.1	76.4	14	13	—	—
0.5	130	31	21	—	—
1	161	46	32	29	20
5	257	109	80	91	71
10	310	150	110	141	113
50	460	294	236	366	306
100	541	378	311	520	435
500	763	615	523	1157	964
1000	871	740	634	1630	1350

NOTE: $B_{12} = B/(10^{12} \text{ G})$. Q_1 is the ionization energy of H atom, Q_2 is the dissociation energy of H₂, and Q_∞ is the cohesive energy of 1d H chain. The superscript “(∞)” implies infinite proton mass. The given numerical results are generally accurate to within 10%. Calculations of Q_∞ are not reliable for $B_{12} \lesssim 1$.

Q_2 and Q_∞ are presented in §§2.2-2.4. Results (without zero-point energy correction) for $N = 3, 4$ have also been given in Paper I. While accurate energies for larger molecules are needed in order to establish the proper scaling of Q_N as a function of N and B , we note the following trend: The ratio Q_2/Q_∞ (and to some extent Q_3/Q_∞) decreases appreciably with increasing B , but Q_N/Q_∞ varies little with B for large N . For a given B , the ratio Q_N/Q_∞ reaches a maximum near $N \sim N_s$ (the saturation point) and then approaches unity from above for $N \gg N_s$.

For the phase equilibrium between the condensed metal and H_N molecules in the vapor (§4) we will need the “surface energy” S_N , defined as the energy release in converting the 3d condensate H_{s,∞} and a H_N molecule into H_{s,∞+N}. Clearly $S_1 = Q_s = (\alpha + 1)Q_\infty$ is the cohesive energy defined in §§2.3-2.4. For linear H_N molecule with energy (per atom) $E_N = E(\text{H}_N)$, we have

$$S_N = N(E_N - E_s) = N\Delta E_s + N(E_N - E_\infty) = N\alpha Q_\infty + fQ_\infty, \quad (2.17)$$

where the first term on the right-hand side comes from cohesive binding between chains, and the second term is the “end energy” of a 1d chain. For $N \geq 2$, we can express S_N in terms of Q_N ’s via

$$S_N = NQ_s - \sum_{i=2}^N Q_i = N\alpha Q_\infty + \left[Q_\infty + \sum_{i=2}^N (Q_\infty - Q_i) \right]. \quad (2.18)$$

The dimensionless factor f in Eq. (2.17) is of order unity: For $N = 4$, it equals 0.23, 0.6, 1.1 and 1.6 for $B_{12} = 1, 10, 100$ and 500, respectively. The asymptotic values of f for $N \gg N_s$ should be close to these values (since $Q_N \rightarrow Q_\infty$ for $N \gg N_s$).

Since $\alpha \sim 0.01$, representing the cohesion between infinite chains, is so small, the first term in equation (2.17) is appreciable only when $N \gtrsim \alpha^{-1} \sim 100$. In that case, the molecular

configuration which minimizes the surface energy S_N of the condensed metal is not a linear chain, but some highly elongated “cylindrical droplet” with N_\perp parallel chains each containing N_\parallel atoms with $N_\perp N_\parallel = N$. For such a droplet, the “end energy” is of order $N_\perp f Q_\infty$. On the other hand there are $\sim \sqrt{N_\perp}$ “unpaired” chains in such a droplet, each gives an energy $N_\parallel \alpha Q_\infty$. Thus the total surface energy is of order $[N_\perp f + \alpha(N/N_\perp)\sqrt{N_\perp}] Q_\infty$. The minimum surface energy S_N , for a fixed $N \gtrsim 2f\alpha^{-1} \equiv N_c$, is then obtained for $N_\perp \simeq (N/N_c)^{2/3}$, $N_\parallel \simeq N^{1/3} N_c^{2/3}$, and is of order

$$S_N \simeq 3f \left(\frac{N}{N_c} \right)^{2/3} Q_\infty, \quad \text{for } N \gtrsim N_c \equiv \frac{2f}{\alpha} \sim 200. \quad (2.19)$$

Thus, although the optimal droplets are highly elongated, the surface energy of the condensed metal still grows as $(N/200)^{2/3}$ for $N \gtrsim 200$.

2.6 Other Species: H^- and H_2^+

For completeness, here we also give fitting formulae for the binding energies of the negative ion H^- and the molecular ion H_2^+ . The energy release in $\text{H} + e = \text{H}^-$ is

$$Q(\text{H}^-) \simeq 0.014 (\ln b)^2 \text{ (a.u.)} \quad (2.20)$$

Thus the ionization energy of H^- is 13 eV for $B_{12} = 1$ and 24 eV for $B_{12} = 10$, as compared to its value of 0.75 eV for $B = 0$. The energy release in $\text{H} + p = \text{H}_2^+$ is

$$Q(\text{H}_2^+) \simeq (0.008 + 0.11 \ln b) (\ln b)^2 \text{ (a.u.)} \quad (2.21)$$

Equations (2.20)-(2.21) are both accurate to within 20%.

Because of the small binding energies, both H^- and H_2^+ are likely to have negligible abundance in a typical neutron star atmosphere. However, the H^- ion might, in principle, contribute appreciably to the atmospheric opacity.

3. THE SAHA EQUILIBRIUM AND WARM ATMOSPHERES

We now consider the physical conditions and chemical equilibrium in neutron star atmospheres with photospheric temperature in the range $T_{\text{ph}} \sim 10^5 - 10^{6.5}$ K and magnetic field strength in the range $B_{12} \sim 0.1 - 20$. These conditions are likely to be satisfied by most observable neutron stars. For such relatively low field strengths, the atmosphere consists mainly of ionized hydrogen, H atoms and small H_N molecules, and we can neglect the condensed metallic phase in the photosphere. Although the density scale height of the atmosphere is only $h \simeq kT_{\text{ph}}/m_p g \simeq 0.08 T_{\text{ph},5} g_{14}^{-1}$ (cm), where $T_{\text{ph},5} = T_{\text{ph}}/(10^5 \text{ K})$, g is surface gravitational acceleration, $g_{14} = g/(10^{14} \text{ cm s}^{-2})$, the atmosphere has significant optical depth. In §4 we shall consider more extreme situation ($B_{12} \gg 10$) when the non-degenerate atmosphere has negligible optical depth and the condensed metallic phase becomes important.

Although the surface layers we consider can lie somewhat below the photosphere, we shall restrict to densities smaller than the zero-pressure condensate density (cf. §2.3)

$$\rho_{s,0} \simeq 560 B_{12}^{6/5} \text{ (g cm}^{-3}\text{)}. \quad (3.1)$$

Thus the density is always below the critical ‘‘Landau density’’ (cf. Eq. [2.6])

$$\rho_{\text{Landau}} = 7.08 \times 10^3 \mu_e B_{12}^{3/2} \text{ (g cm}^{-3}\text{)}, \quad (3.2)$$

where μ_e is the mean molecular weight per electron ($\mu_e = 1$ for ionized hydrogen). For our ranges of B and T_{ph} we also have the inequality $T \ll \hbar\omega_e/k = 1.34 \times 10^8 B_{12}$ K, so that all electrons settle in the ground Landau state. The electron Fermi temperature $T_F = E_F/k$ is then given by

$$T_F = 2.67 B_{12}^{-2} \left(\frac{\rho}{\mu_e} \right)^2 \text{ (K)}, \quad (3.3)$$

where ρ is the mass density in g cm^{-3} . At the density of the condensate (Eq. [3.1]), we would have $T_F \simeq 8.4 \times 10^5 B_{12}^{2/5}$ K; but for ρ much smaller than $\rho_{s,0}$, we have $T_{\text{ph}} \gg T_F$, and the electrons are nondegenerate.¹

3.1 The Photospheric Density and Pressure

In a star with an interior energy source (such as an isolated cooling neutron star), the photon flux $F = \sigma_{\text{sb}} T_{\text{eff}}^4$ is constant to very far below the photosphere (σ_{sb} is the Stefan-Boltzmann constant). With an accretion energy source, this constancy holds only above the stopping layer for the infalling matter. However, the optical depth τ_{stop} in this layer is much larger than unity for a warm atmosphere², and we shall consider only optical depth τ less than τ_{stop} , where $\tau = \int \kappa dy$ with κ the Rosseland mean opacity and $y = \int \rho dz$ the column density. With the flux $F = \sigma_{\text{sb}} T_{\text{eff}}^4$ assumed constant, a simple approximation for the temperature profile $T(\tau)$ is

$$T^4(\tau) \simeq \frac{3}{4} T_{\text{eff}}^4 \left(\frac{2}{3} + \tau \right), \quad (3.4)$$

and the photospheric temperature $T_{\text{ph}} = T_{\text{eff}}$ (with τ_{ph} chosen as 2/3). With the gravitational acceleration g in the atmosphere constant, hydrostatic equilibrium gives for the pressure $P = gy$ and, rewriting $\tau = \bar{\kappa}y$, we have

$$P(\tau) = \frac{g}{\bar{\kappa}} \tau; \quad P_{\text{ph}} \simeq \frac{2g}{3\bar{\kappa}}. \quad (3.5)$$

Note that Eq. (3.5) holds irrespective of the equation of state, even when there is a phase transition at some pressure (see §4). For the warm atmospheres considered in this section, the ideal gas law applies and the photospheric density is given by $\rho_{\text{ph}} \simeq P_{\text{ph}} m_p / (k T_{\text{ph}})$.

For the temperature and density relevant to the atmosphere, free-free absorption dominates over electron scattering. In the zero-field case, assuming Kramer’s opacity $\kappa(0) = \kappa_0 \rho T^{-3.5}$, with $\kappa_0 \simeq 7.4 \times 10^{22}$ (cgs), we would obtain the photosphere density-temperature

¹ Equation (3.3) should be compared with the Fermi temperature in field-free case, $T_F(0) = 3.0 \times 10^5 (\rho/\mu_e)^{2/3}$ (K). Clearly, high magnetic field lifts the degeneracy of electrons even at relatively high density.

² The column density y_{stop} of the stopping layer typically corresponds to a few to tens of Thompson depths (depending on the field strength), i.e., $y_{\text{stop}} \sim 10/\kappa_{\text{es}}$, where κ_{es} is the electron scattering opacity (cf. Nelson et. al. 1993). Thus for an absorption-dominated atmosphere, $\tau_{\text{stop}} \sim 10\bar{\kappa}_{\text{ff}}/\kappa_{\text{es}} \gg 1$.

relation $\rho_{\text{ph}}(0) \simeq 7 \times 10^{-3} g_{14}^{1/2} T_{\text{ph},5}^{5/4} \text{ g cm}^{-3}$. In a strong magnetic field, the radiative opacity becomes anisotropic and depends on polarization (Canuto et al. 1971; Lodenquai et al. 1974; Pavlov et al. 1994). For photons with polarization vector perpendicular to the magnetic field (the “extraordinary mode”) the free-free absorption and electron scattering opacities are reduced below their zero-field values by a factor of $(\omega/\omega_e)^2$, while for photons polarized along the magnetic field (the “ordinary mode”), the opacities are not affected. Silant’ev and Yakovlev (1980) have calculated the appropriate average Rosseland mean free-free opacity. In the field and temperature regime of interest, an approximate fitting formula is

$$\kappa(B) \simeq 400 \beta \left(\frac{kT}{\hbar\omega_e} \right)^2 \kappa(0), \quad (3.6)$$

with $\beta \simeq 1$. The resulting photosphere density and pressure are given by

$$\begin{aligned} \rho_{\text{ph}}(B) &\simeq 0.5 \beta^{-1/2} g_{14}^{1/2} T_{\text{ph},5}^{1/4} B_{12} \text{ (g cm}^{-3}\text{)}, \\ P_{\text{ph}}(B) &\simeq 4 \times 10^{12} \beta^{-1/2} g_{14}^{1/2} T_{\text{ph},5}^{5/4} B_{12} \text{ (dyne cm}^{-2}\text{)}. \end{aligned} \quad (3.7)$$

In Figure 2, this photosphere ($\tau \simeq 2/3$) condition is shown in a temperature-density diagram. For $\beta \sim 1/400$, equation (3.7) also approximately characterizes the physical conditions of the deeper layer where the extraordinary photons are emitted. This “ $\tau_{\perp} \simeq 2/3$ ” line is also shown in Figure 2. Solving Eqs. (3.4)-(3.5) (more precisely, $dP/d\tau = g/\kappa$), we can obtain the temperature profile of the atmosphere as a function of density. Some of such $T - \rho$ profiles for different values of $T_{\text{eff}} = T_{\text{ph}}$ are depicted in Figure 2. Clearly, $T \rightarrow T_{\text{ph}}/2^{1/4} = 0.84T_{\text{ph}}$ as $\tau \rightarrow 0$, while $T \propto \tau^{1/4} \propto \rho^{4/9}$ as $\tau \rightarrow \infty$.

Other sources of opacity such as bound-free and bound-bound absorptions will increase the opacity and reduce the photosphere density, but the above estimates define the general range of the physical parameters in the atmosphere if T_{eff} is large enough for the neutral H abundance to be small. This rough estimates agree reasonably well with more detailed calculations of Pavlov et al. (1995).

3.2. Ionization Saha Equilibrium

We now consider the ionization-recombination equilibrium of the H atom. Previous treatments of this problem (e.g., Khersonskii 1987; Miller 1992) have assumed that the H atom can move across the magnetic field freely. This is generally not valid for the strong field regime of interest here. A free electron confined to the ground Landau level, the usual case for $b \gg 1$, does not move perpendicular to the magnetic field. Such motion is necessarily accompanied by Landau excitations. When the electron combines with a proton, the mobility of the neutral atom across the field depends on the ratio of the atomic excitation energy ($\sim \ln b$) to the Landau excitation energies $\hbar\omega_p = \hbar eB/(m_p c)$ for the proton. It is convenient to define a critical field strength B_{crit} via

$$b_{\text{crit}} \equiv \frac{m_p}{m_e} \ln b_{\text{crit}} = 1.80 \times 10^4; \quad B_{\text{crit}} = b_{\text{crit}} B_o = 4.23 \times 10^{13} \text{ G}. \quad (3.8)$$

Thus for $B \gtrsim B_{\text{crit}}$, the deviation from the free center-of-mass motion of the atom is significant (Paper III).

In a strong magnetic field, the center-of-mass motion of the atom is specified by a pseudomomentum \mathbf{K} , whose component along the field axis is simply the usual liner momentum,

while the perpendicular component \mathbf{K}_\perp measures the mean transverse separation of the electron and proton (Avron, Herbst & Simon 1978; Herold, Ruder & Wunner 1981; Paper III and references therein). For a H atom in the ground state, the total energy (in atomic units) is approximately given by (Paper III)

$$\mathcal{E}_0(K_z, K_\perp) \simeq \frac{K_z^2}{2M} - |E(\text{H})| + \frac{K_c^2}{2M_\perp} \ln \left(1 + \frac{K_\perp^2}{K_c^2} \right), \quad (3.9)$$

where we have defined

$$M_\perp \simeq M \left(1 + \frac{\xi b}{Ml} \right) \simeq M \left(1 + \frac{\xi b}{b_{\text{crit}}} \right), \quad K_c^2 \simeq 0.64 \xi b \left(1 + \frac{Ml}{\xi b} \right)^2, \quad (3.10)$$

and $M = m_p + m_e \simeq m_p/m_e$ (a.u.), $\xi \simeq 2.8$, $|E(\text{H})| \simeq 0.16 l^2$ (a.u.) (cf. Eqs. [2.1]-[2.2]). Note that for $K_\perp \ll K_c$, the dependence of \mathcal{E}_0 on K_\perp becomes $K_\perp^2/(2M_\perp)$. Thus M_\perp represents the effective mass for the transverse motion across the magnetic field. Potekhin (1994) has given more accurate numerical results for a few selected field strength, but the approximation in equation (3.9) is adequate for our purpose.

Let the proton (free or bound) number density in the gas be n_g . The partition function (in atomic units) for a H atom in a volume $V_g = 4\pi r_g^3/3 = 1/n_g$ is then

$$Z(\text{H}) \simeq V_g \left(\frac{MT}{2\pi} \right)^{1/2} \frac{M'_\perp T}{2\pi} \exp \left(\frac{|E(\text{H})|}{T} \right) z(\text{H}), \quad (3.11)$$

where

$$M'_\perp = M_\perp \left(1 - \frac{2M_\perp T}{K_c^2} \right)^{-1} \quad (3.12)$$

for $T \ll K_c^2/(2M_\perp)$, and M'_\perp/M_\perp approaches a constant less than unity when T becomes comparable to $K_c^2/(2M_\perp)$. The partition function $Z(\text{H})$ has the same form as the zero-field expression except for the factor M'_\perp/M . In equation (3.11), $z(\text{H}) = z_m(\text{H})z_\nu(\text{H})$, where $z_m(\text{H})$ is the internal partition function associated with the $m > 0$ excited states:

$$z_m(\text{H}) \simeq \left(1 + e^{-b/MT} \right) \sum_{m=0}^{m_{\text{max}}} \frac{M'_{\perp m}}{M'_\perp} \exp \left[-\frac{1}{T} \left(0.16 l^2 + E_m + m \frac{b}{M} \right) \right], \quad (3.13)$$

where $M'_{\perp m}$ is of the same order of magnitude as M'_\perp , the factor $(1 + e^{-b/MT})$ comes from the proton spin effects, and m_{max} is set by the condition $L_\perp \lesssim r_g$ or $L_z \lesssim r_g$ (cf. §2.1). The internal partition function z_ν associated with the $\nu > 0$ states is close to unity (see Paper III for detail).

The partition functions for the ionized states (free electron and proton) can be easily obtained. With the atomic bound-state partition function given above, we can obtain the generalized Saha equation for the ionization-recombination equilibrium in the presence of strong magnetic field. In the density and temperature regimes of interest, with $T \lesssim K_c^2/(2M_\perp) \simeq 0.32 l (1 + Ml/\xi b)$, we have

$$\frac{n(\text{H})}{n_p n_e} \simeq \left(\frac{b}{2\pi} \right)^{-2} M'_\perp \left(\frac{T}{2\pi} \right)^{1/2} \tanh \left(\frac{b}{2MT} \right) \tanh \left(\frac{b}{2T} \right) \exp \left(\frac{Q_1}{T} \right) z(\text{H}), \quad (3.14)$$

where $n(\text{H})$, n_p and n_e are the number densities of the different species.

3.3 Dissociation Equilibrium of Molecules

Accurate treatment of the dissociation equilibrium for H_N molecules is complicated. However, since the molecular excitation energies are comparable to the excitations in H atom (§2.2), we expect that when $T \lesssim K_c^2/(2M_\perp) \sim l(1 + Ml/\xi b)$, we can similarly use an effective mass description for the motion of the molecule across the magnetic field. As an estimate, we assume that the effective mass of H_N molecule is $M_\perp(\text{H}_N) \sim NM(1 + \xi b/Ml)$. We similarly introduce the correction factor M'_\perp/M_\perp given in equation (3.12). The Saha equation for the equilibrium process $\text{H}_N + \text{H} = \text{H}_{N+1} + Q_{N+1}$ is then given by

$$\frac{n(\text{H}_{N+1})}{n(\text{H}_N)n(\text{H})} \simeq \left(\frac{N+1}{N}\right)^{3/2} \left(\frac{MT}{2\pi}\right)^{-3/2} \left(\frac{M}{M'_\perp}\right) \exp\left(\frac{Q_{N+1}}{T}\right) \frac{z(\text{H}_{N+1})}{z(\text{H}_N)z(\text{H})}, \quad (3.15)$$

where $z(\text{H}_{N+1})$, $z(\text{H}_N)$, $z(\text{H})$ are the internal partition functions of H_{N+1} , H_N , H respectively. To estimate the internal partition functions of the molecules, one need to include various molecular excitation levels as discussed in §2.2. But presumably the ratio of these internal partition functions is of order unity (this approximation is adopted in the calculations presented in §3.5), since the molecular excitation level spacing is not necessarily smaller than the electronic excitation (§2.2).

3.4 Non-ideal Gas Effect

So far we have assumed the gas to be sufficiently dilute to be treated as an ideal gas. When the gas density increases, the interaction between particles becomes important. The effect of the atom-atom interaction potential $U_{12}(r)$ on the ionization equilibrium is to modify the chemical potential of the atomic gas by the amount

$$\Delta\mu(\text{H}) = n(\text{H})kT \int d^3r (1 - e^{U_{12}/kT}), \quad (3.16)$$

(e.g., Landau & Lifshitz 1980). For r much larger than the atomic length $L_z \sim 1/l$ of the elongated atom, the potential U_{12} is due to the quadrupole-quadrupole interaction $U_{12} \sim Q^2(3 - 30\cos^2\theta + 35\cos^4\theta)/r^5$, where θ is the angle between the vector \mathbf{r} and the z -axis, and $Q \sim eL_z^2$ is the quadrupole moment of the atom. Since the integration over the solid angle $\int d\Omega U_{12} = 0$ at large r , the contribution to $\Delta\mu(\text{H})$ from large r is negligible. The main effect is then the “excluded volume effect”: Let v_a be the volume of the (highly non-spherical) electron distribution for one atom, so that we can set $U_{12} \rightarrow \infty$ due to quantum mechanical repulsion when two atoms overlap. We then have $\Delta\mu(\text{H}) \sim kTn(\text{H})v_a$. The atom-atom interaction introduces a factor $\exp(-\Delta\mu/kT) \sim \exp(-nv_a)$ to the right-hand-side of the Saha equation (3.14). Therefore when the mean density in the gas becomes comparable to the internal density of the atom, the atom is mostly ionized — so called *pressure ionization*. One can similarly consider the interaction between a charged particle (electron or proton) and the atom, given by the quadrupole-monopole potential $U_{12} \sim eQ(3\cos^2\theta - 1)/r^3$. Again since $\int d\Omega U_{12} = 0$, the long-range term is negligible. We thus obtain a similar factor of order $\sim \exp(-nv_a)$ correction to the Saha equation.

The “atomic volume” v_a is of order $\pi L_\perp^2 L_z$, where $L_\perp \sim b^{-1/2}$ is the radius perpendicular to the z -axis and $L_z \sim 1/l$ the length in the z -direction. The ratio of this volume to the volume per electron in the condensed state, $4\pi r_{s,0}^3/3$ with $r_{s,0}$ given in equation

(2.8), is then $\sim 0.1 b^{1/5} / \ln b$, which increases slowly with increasing b and is of order 0.1 for $B_{12} \sim 1 - 10^3$. The “excluded volume” of the atom may be larger due to its elongated shape, but $v_a \lesssim L_z^3 \sim 4\pi r_{s,0}^3/3$. Thus we have $\Delta\mu(\text{H}) \sim kT(\rho/\rho_{s,0})$, where $\rho_{s,0}$ given by Eq. (3.1). The corresponding pressure-ionization factor in the Saha equations is $\exp(-\Delta\mu/kT)$.

3.5 Results

To get a qualitative overview of the relative abundances of different forms of hydrogen, we have determined the H atom half-ionization and H₂ half-dissociation curves in the $T - \rho$ diagram. In Figure 2, we show the results for $B_{12} = 1$ and $B_{12} = 10$; we also plot the electron degeneracy line ($T = T_F$) and the typical photosphere conditions (§3.1). The half-ionization line is determined by setting $n_e/n_g = n_p/n_g = n(\text{H})/n_g = 1/2$, while the half-dissociation line is obtained with $n(\text{H})/n_g = 1/2$ and $n(\text{H}_2)/n_g = 1/4$ (so that H and H₂ have equal mass fractions). Note that the gas density is simply $\rho = m_p n_g$, and the pressure ionization factor discussed in §3.4 is not included in the calculations. To the left of the half-ionization line (labeled “e+p=H”) the atmosphere is mostly ionized, while to the right of the half-dissociation line (labeled “H+H=H₂”), most of the material is in the molecular states, H₂, H₃, etc. Between the ionization line and the H₂ dissociation line, the dominant species is H atom. From Eqs. (3.7) and (3.14), we can obtain the photospheric “ionization temperature”, $T_{\text{ph,ir}}$, where the ionization-recombination equilibrium gives 50% H and 50% e+p in the photosphere ($\tau = 2/3$). For $B_{12} \sim 1 - 50$, an approximate fitting formula is

$$\log_{10} T_{\text{ph,ir}} \simeq 5.4 + 0.3 \log_{10} B_{12}. \quad (3.17)$$

If the actual photospheric temperature T_{ph} is greater than $T_{\text{ph,ir}}$, then there is little neutral H near and above the photosphere ($\tau \lesssim 1$), and the neutral abundance increases slowly with depth. If T_{ph} is only slightly smaller than $T_{\text{ph,ir}}$, then neutral H dominates in layers near the photosphere ($\tau \sim 1$), but (e+p) dominates at higher levels ($\tau \ll 1$), because T is almost constant for $\tau \lesssim 1$ while ρ decreases to zero as $\tau \rightarrow 0$ (cf. Fig. 2). For $B_{12} = 1$, the abundances of molecular species are negligible unless the photospheric temperature drops well below 10^5 K. For $B_{12} = 10$, there exists a large amount of H₂ in the photosphere when $T_{\text{ph},5} \lesssim 2$.

The “neutrality fraction” $n(\text{H})/n_g$ as a function of temperature at a fixed density $\rho = n_g m_p = 0.01$ g/cm³ and 0.1 g/cm³ is shown in Fig. 3. Results for a wide range of field strengths ($B_{12} = 0.01, 0.1, 1, 10$) are given and compared with the zero-field limit. In general, the neutral fraction is not a monotonic function of B , because it is determined by two opposite effects [cf. Eq. (3.14)]: the ionization energy Q_1 increases with increasing B , this tends to increase $n(\text{H})/n_g$; on the other hand, the phase space of free electron and proton, proportional to $b^2/\tanh(b/2MT)$, also increases with increasing B , and this tends to decrease $n(\text{H})/n_g$. It is also easy to understand from Eq. (3.14) that the neutral fraction is in general a non-monotonic function of T at a given field strength. As seen from Fig. 3, even a relatively small field increases the neutrality appreciably above the field-free value, partly because Q_1 is larger, but also because the internal partition function $z_m(\text{H})$ is larger. Thus it may well be that a $B = 10^9 - 10^{10}$ G atmosphere (which characterizes millisecond pulsars) is very different from a field-free atmosphere (Rajagopal & Romani 1996; Zavlin et al. 1996).

Figure 4 shows the fraction (by number) of various hydrogen gas species as a function of T_{ph} at a point with $P = 0.5P_{\text{ph}}$ (cf. Eq. [3.7] with $\beta = 1$ and $g_{14} = 1$), $\tau = 1/3$ and $T = (3/4)^{1/4} T_{\text{ph}} = 0.93 T_{\text{ph}}$. Three magnetic field strengths ($B_{12} = 1, 10, 100$) are considered. The total number density n_{tot} of free particles in the gas, i.e., $n_{\text{tot}} = n_e + n_p +$

$n(\text{H}) + n(\text{H}_2) + \dots$, is given by $n_{\text{tot}} = P/kT = 1.6 \times 10^{23} B_{12} T_{\text{ph},5}^{1/4}$ (cm^{-3}). Neglecting the trace ion species such as H^- and H_2^+ (and the condensed phase), the abundances satisfy the condition $2X_p + X(\text{H}) + X(\text{H}_2) + X(\text{H}_3) + \dots = 1$, where $X_p = n_p/n_{\text{tot}}$ and $X(\text{H}_N) = n(\text{H}_N)/n_{\text{tot}}$. For determining X_p , $X(\text{H})$, $X(\text{H}_2)$, the values of Q_1 , Q_2 given in Table 1 are used, while for determining the fractions of larger molecules, the following approximate *ansatz* is adopted in our calculation (cf. §2.5): For H_3 and H_4 , the ratio $Q_N^{(\infty)}/Q_\infty^{(\infty)}$ given in Paper I is assumed, and the zero-point energy correction to Q_N is introduced by setting $Q_N = (Q_N^{(\infty)}/Q_\infty^{(\infty)})Q_\infty$ with Q_∞ given in Table 1; For $N > 4$, where no numerical result is currently available, we simply set $Q_N = Q_\infty$. Clearly, the uncertainty is largest for intermediate-sized molecules ($N \sim N_s$), but we have checked that moderate variations (less than 30%) of these intermediate Q_N 's do not change our results significantly. The approximation should become better for $N \gg N_s$ as Q_N asymptotes to Q_∞ . For $B_{12} = 1, 10$, we see that the atmosphere is dominated by atoms and relatively small molecules, and the total gas density $\rho = m_p n_g = m_p [n_p + n(\text{H}) + 2n(\text{H}_2) + 3n(\text{H}_3) + \dots]$ remains much less than the condensation density $\rho_{s,0}$. For the extreme field strength $B_{12} = 100$, which we include here for illustrative purpose, increasingly large molecules dominate the atmosphere as T_{ph} decreases, and the gas density approaches $\rho_{s,0}$. This is indicative of a phase transition which will be discussed in §4.

For layers deeper than the photosphere, i.e., for optical depth τ increasing to large values, the ionization fraction changes slowly since the temperature-density track in the atmosphere, $\rho \propto T^{9/4}$ (for $\tau \gg 1$), is close to the track of constant (e+p)/H ratio. Indeed, from Fig. 2 we see that the ionization fraction varies by only a factor of a few below the photosphere. The zero-pressure density $\rho_{s,0}$ of the condensed metal is given by Eq. (3.1) and shown by the heavy vertical lines in Figure 2. Note that the half-ionization lines and half-dissociation lines are meaningful only in the density regime to the left of the condensation density lines and the degeneracy lines. When τ is sufficiently large that ρ approaches $\rho_{s,0}$, non-ideal gas effects and/or condensation set in. With $T \propto \rho^{4/9}$, the temperature at $\rho \sim \rho_{s,0}$ is of order $T \sim 20 T_{\text{ph}}$. For a warm atmosphere this exceeds the critical temperature for phase transition, $T_{\text{crit}} \sim 10^5 B_{12}^{0.4}$ K (see §4). Thus there is no distinct condensed phase, although the atoms would overlap at $\rho \gtrsim \rho_{s,0}$ and be pressure-ionized. The electrons form a uniform fluid, but stay in the ground Landau level until ρ exceeds ρ_{Landau} (the dot-dashed vertical lines in Fig. 2).

4. ULTRAHIGH FIELDS AND COOL ATMOSPHERES: THE CONDENSED PHASE

As discussed in §2, the cohesive energy Q_s and surface energy S_N of the condensed metallic hydrogen increase more rapidly with increasing field strength than the ionization energy Q_1 of H atom and the dissociation energy Q_N of small H_N molecules (cf. Fig. 1). We shall see below (cf. Eqs. [4.5]-[4.7]) that $Q_s = S_1$, S_N and $(Q_s + Q_1)/2$ determine the partial saturation vapor densities of H, H_N and (p+e) respectively. For $B_{12} \gg 10$, the cohesive energy is greater than Q_1 and Q_2 , and is close to $|E_{s,0}| \simeq 8 B_{12}^{0.4}$ a.u. In this case there may exist a critical temperature T_{crit} , below which there is a first order phase transition between the condensed metallic hydrogen³ and the gaseous vapor. We explore the possibility of this

³ The condensed metal may be solid or liquid. Using the zero-field criterion as an estimate, the melting temperature is determined by $\Gamma = e^2/(r_s kT) = 18.7 B_{12}^{2/5}/T_5 \simeq 180$, where we

phase separation and the partial saturation vapor pressure of various constituents in this section.

4.1 Phase Equilibrium Conditions

Consider the equilibrium between the condensed metallic phase (labeled by the subscript “s”) and the non-degenerate gaseous phase (labeled by “g”). The electron number density in the metallic phase is $n_s = 1/V_s = 3/(4\pi r_s^3)$, where r_s is the mean proton spacing (the radius of Wigner-Seitz cell). The gaseous phase consists of a mixture of free electrons, protons, bound atoms and molecules, with the total baryon number density $n_g = 1/V_g = n_p + n(\text{H}) + 2n(\text{H}_2) + \dots$. We neglect the small concentration of H^- , H_2^+ and other molecular ions in the gas, thus we have $n_e = n_p$. Phase equilibrium requires the temperature, pressure and the chemical potentials of different species to satisfy the conditions:

$$\begin{aligned} T_s &= T_g = T, \\ P_s &= P_g = [2n_p + n(\text{H}) + n(\text{H}_2) + n(\text{H}_3) + \dots]kT = P, \\ \mu_s &= \mu(\text{H}) = \mu_e + \mu_p = \frac{1}{2}\mu(\text{H}_2) = \frac{1}{3}\mu(\text{H}_3) = \dots \end{aligned} \quad (4.1)$$

First consider the equilibrium between the condensed metal and H atoms in the gaseous phase. Near the zero-pressure metal density, the electron Fermi temperature is $T_{F,0} \simeq 8.4 \times 10^5 B_{12}^{2/5}$ K (cf. Eqs. [3.1], [3.3]). Thus at a given temperature, the metal becomes more degenerate as B increases. Let the energy per Wigner-Seitz cell be $E_s(r_s)$. The pressure and chemical potential of the condensed phase are given by

$$P_s = -\frac{1}{4\pi r_s^2} \frac{dE_s}{dr_s}, \quad \mu_s = E_s(r_s) + P_s V_s \simeq E_{s,0} + P_s V_{s,0}, \quad (4.2)$$

where the subscript “0” indicates the zero-pressure values, and we have assumed that the vapor pressure is sufficiently small so that the deviation from the zero-pressure state of the metal is small, i.e., $\delta \equiv |(r_s - r_{s,0})/r_{s,0}| \ll 1$. This is justified when the saturation vapor pressure P_{sat} is much less than the critical pressure P_{crit} for phase separation, or when $T \ll T_{\text{crit}}$. The finite temperature correction $\Delta\mu_s$ to the chemical potential of the condensed phase is given by ⁴

$$\frac{\Delta\mu_s(T)}{kT} \simeq \frac{\pi^2}{12} \frac{T}{T_F} \simeq 0.10 B_{12}^{-2/5} T_5, \quad \Delta\mu_s(T) \simeq 0.85 B_{12}^{-2/5} T_5^2 \text{ (eV)}, \quad (4.3)$$

where the Fermi energy $E_F = kT_F = 9\pi^2/(8b^2 r_s^6) \simeq 0.236 b^{2/5}$ (a.u.), and for the density we have used the zero-pressure value. The partition function of H atoms is given by equation (3.11). Using $n(\text{H}) = \exp[\mu(\text{H})/T]Z(\text{H})/V_g$ and the equilibrium condition $\mu(\text{H}) = \mu_s$, we obtain the number density of H atoms in the saturated vapor:

$$n(\text{H}) \simeq \left(\frac{MT}{2\pi}\right)^{3/2} \left(\frac{M'_\perp}{M}\right) z(\text{H}) \exp\left[\frac{-Q_s + PV_{s,0} + \Delta\mu_s(T) - \Delta\mu(\text{H})}{T}\right], \quad (4.4)$$

have used the zero-pressure value for r_s given by Eq. (2.8). Thus for $B_{12} \lesssim 287 T_5^{5/2}$ the zero-pressure metal is likely to be a liquid.

⁴ For $kT \ll \hbar\omega_e$ and $E_F \ll \hbar\omega_e$ so that electrons are all in the ground Landau level, we have $n_s = (2eB/h^2c) \int_0^\infty dp_z \{\exp[(p_z^2/2m_e - \mu)/kT] + 1\}^{-1} \simeq (2eB/h^2c)(2m_e\mu)^{1/2} [1 - (\pi kT)^2/(24\mu^2)]$, which gives $\mu \simeq E_F [1 + (\pi kT)^2/(12E_F^2)]$. Note that this correction has the same form as that for a non-magnetic electron gas, but with opposite sign.

where the cohesive energy $Q_s = |E_{s,0}| - |E(\text{H})|$ is given by equation (2.16). Since $PV_{s,0}$ is typically much smaller than the cohesive energy Q_s , and for low vapor density we can neglect the non-ideal gas correction $\Delta\mu(\text{H})$, equation (4.4) reduces to an explicit expression for $n(\text{H})$:

$$n(\text{H}) \simeq \left(\frac{MT}{2\pi}\right)^{3/2} \left(\frac{M'_\perp}{M}\right) z(\text{H}) \exp\left(\frac{-Q_s + \Delta\mu_s}{T}\right). \quad (4.5)$$

The densities of the other species in the saturated vapor can also be obtained. Equation (4.5) together with the Saha equation for $e+p=\text{H}+Q_1$ (Eq. [3.14]) yields

$$n_p \simeq \frac{bM^{1/4}T^{1/2}}{(2\pi)^{3/2}} \left[\tanh\left(\frac{b}{2MT}\right)\right]^{-1/2} \exp\left(\frac{-Q_1 - Q_s + \Delta\mu_s}{2T}\right). \quad (4.6)$$

The partition function of H_N molecules can be approximated by

$$Z(\text{H}_N) = V_g \left(\frac{NMT}{2\pi}\right)^{3/2} \left(\frac{M'_\perp}{M}\right) z(\text{H}_N) \exp\left(-\frac{NE_N}{T}\right),$$

(cf. §3.3, and recall that E_N is the energy per atom in a H_N molecule). The equilibrium condition $N\mu_s = \mu_N$ for the process $\text{H}_{s,\infty} + \text{H} = \text{H}_{s,\infty+N}$ (with energy release $S_N = NE_N - NE_s$, where S_N is the surface energy discussed in §2.5.) would then give $n(\text{H}_N) = \exp(\mu_N/T)Z(\text{H}_N)/V_g$. For large molecular chains ($N \gg N_s$) or droplets ($N \gtrsim N_c$; cf. §2.5), however, a correction $\Delta\mu_N$ to the “internal” chemical potential due to finite temperature need to be included ($\Delta\mu_N$ is to be distinguished from the non-ideal gas correction discussed in §3.4). For large 3d droplets, this correction is identical to that given in Eq. (4.3), i.e., $\Delta\mu_N = N\Delta\mu_s$. For linear chains with $N \gg N_s$, we expect that $\Delta\mu_N/N$ is still close to $\Delta\mu_s$ since electrons behave like a Fermi gas in the molecular chain as they do in 3d condensate, although it is not clearly which is greater.⁵ We therefore write $\Delta\mu_N = \zeta N\Delta\mu_s$, with $\zeta \simeq 0$ for $N \lesssim N_s$ and $\zeta \simeq 1$ for $N \gg N_s$. With this correction, the saturated density of H_N is given by

$$n(\text{H}_N) \simeq N^{3/2} \left(\frac{MT}{2\pi}\right)^{3/2} \left(\frac{M'_\perp}{M}\right) z(\text{H}_N) \exp\left[\frac{-S_N + N(1-\zeta)\Delta\mu_s}{T}\right]. \quad (4.7)$$

For concreteness, we shall set $\zeta = 0$ for $N = 1 - 5$ and $\zeta = 1$ for $N > 5$ in our calculations below. This is adequate for our purpose since $N(1-\zeta)\Delta\mu_s$ is typically much less than S_N for small molecules. More detailed (and unknown) prescription for ζ as a function of N (as long as ζ satisfies the asymptotic behavior discussed above) would have negligible effect on our results presented below.

4.2 Critical Temperature for Phase Separation

The critical temperature T_{crit} , below which phase separation between condensed metal and gaseous vapor occurs, is determined by the condition $n_s = n_g = n_p + n(\text{H}) + 2n(\text{H}_2) + 3n(\text{H}_3) + \dots$. In equation (2.17) for the surface energy, the factor f is of order unity, and

⁵ Since the mean electron density in 3d condensate is higher than that in 1d chain by about 0.2% (cf. Appendix A), we may expect that $\Delta\mu_N/N$ is larger than $\Delta\mu_s$ by $\sim 0.4\%$ according to Eq. (4.3).

approaches a constant for $N \gg N_s$. Substituting Eq. (2.17) with $f \sim \text{constant}$ into Eq. (4.7) with the approximation $z(\text{H}_N) \sim z(\text{H})$, we obtain

$$n_g \simeq n_p + \left(\frac{MT}{2\pi}\right)^{3/2} \left(\frac{M'_\perp}{M}\right) z(\text{H}) \exp\left(-\frac{fQ_\infty}{T}\right) \sum_N N^{5/2} \exp\left\{-\frac{N[\alpha Q_\infty - (1-\zeta)\Delta\mu_s]}{T}\right\}. \quad (4.8)$$

Clearly, for the sum to converge, we require $\alpha Q_\infty > (1-\zeta)\Delta\mu_s$. With $\alpha Q_\infty = \Delta E_s \simeq 0.01|E_\infty| \simeq 2 B_{12}^{0.37}$ eV, this reduces to $T_5 \lesssim 1.5 B_{12}^{0.4}/(1-\zeta)^{1/2}$, which is easily satisfied for $T < T_{\text{crit}}$ (see below) and $\zeta \simeq 1$. Thus we neglect $(1-\zeta)\Delta\mu_s$ in comparison to αQ_∞ . The sum in Eq. (4.8) therefore reduces to a finite number of order $\bar{N}^{5/2} [\exp(\alpha Q_\infty/T) - 1]^{-1} \sim \bar{N}^{5/2}$ (recall that $fQ_\infty \gg \alpha Q_\infty$), where $\bar{N} \sim 2.5T/(\alpha Q_\infty)$ specifies the term that contributes most to the sum. The critical temperature for phase transition is then given by

$$T_{\text{crit}} \simeq \frac{fQ_\infty}{\ln \Lambda} \sim 0.1fQ_\infty, \quad \Lambda \equiv n_s^{-1} \left(\frac{MT}{2\pi}\right)^{3/2} \left(\frac{M'_\perp}{M}\right) z(\text{H}) \bar{N}^{5/2}, \quad (4.9)$$

where we have neglected n_p , and in estimating $\ln \Lambda$ we have used $n_s = \rho_s/m_p \simeq 50 B_{12}^{6/5}$ (a.u.) (cf. Eq. [3.1]) and $T_5 \sim 2 B_{12}^{0.4} \sim T_{\text{crit}}$ (which gives $\bar{N} \sim 20$). Thus for $f \simeq 1$, we find $T_{\text{crit}} \simeq 10^5$, 5×10^5 and 10^6 K for $B_{12} = 10$, 100 and 500 respectively (see also Fig. 5). The corresponding critical pressure is of order $P_{\text{crit}} \simeq (n_g/\langle N \rangle)kT_{\text{crit}} \sim 0.1n_s Q_\infty/\langle N \rangle$, where $\langle N \rangle$ is the typical size of molecules in the vapor.

4.3 Saturated Vapor of Condensed Metallic Hydrogen

Figure 5(a)-(c) depicts the partial saturation vapor densities of different species in equilibrium with metallic hydrogen as a function of temperature for $B_{12} = 10$, 100 and 500. These densities are calculated using Eqs. (4.5)-(4.7), where the surface energy $S_N = (N\alpha + f)Q_\infty$ is obtained from Q_N and Q_∞ via Eq. (2.18), and we adopt the same *ansatz* for Q_N as described in §3.5, i.e., we use the numerical results for Q_1, Q_2, Q_3, Q_4 and Q_∞ (the zero-point energy corrections to Q_3 and Q_4 are incorporated via $Q_N/Q_\infty = Q_N^{(\infty)}/Q_\infty^{(\infty)}$), and we set $Q_N = Q_4$ for $N > 4$. This approximation for Q_N corresponds to $f = 0.23, 0.6, 1.1, 1.7$ for $N \geq 4$ at $B_{12} = 1, 10, 100, 500$ respectively. In calculating the total baryon density n_g in the vapor, we include linear molecular chains H_N with N up to $N_{\text{max}} = 200$ [cf. Eq. (2.19)] and neglect “droplets” in the vapor. Choosing a different $N_{\text{max}} \gg 1$ would only change the total vapor density n_g slightly for $T \lesssim T_{\text{crit}}$. The solid vertical line in each panel of Fig. 5 indicates the temperature at which n_g equals n_s . This defines the critical temperature T_{crit} for phase transition, and it is well approximated by $0.1 Q_\infty/k$. Thus $T_{\text{crit}} \simeq 9 \times 10^4, 5 \times 10^5$ and 1.4×10^6 K for $B_{12} = 10, 100$ and 500 respectively. Note that for illustrative purpose, we have considered in Fig. 5(a) relatively low field strength, $B_{12} = 10$, where the condensed phase is more uncertain. This uncertainty for the low-field case is reflected by the fact that $n(\text{H}_2) > n(\text{H})$ in the saturated vapor, so that larger molecules have even greater abundances. Thus there may not be a distinct condensed phase at all, and even if phase separation exists, the condensation temperature is below 10^5 K. In such relatively low- B regime, the outer layer of the neutron star is characterized by *gradual* transformation from nondegenerate gas to degenerate plasma as the pressure (or column density) increases (see §3). For $B_{12} \gg 10$ [cf. Fig. 5(b)-(c)], on the other hand, the vapor density becomes much less than the condensation density as the temperature decreases and/or the magnetic field increases, thus phase separation is inevitable.

The most abundant species in saturated vapor at $T \sim T_{\text{crit}}/2$ (for example) depend on the field strength, with smaller fields favoring poly-atomic molecules since f in Eq. (2.17) is smaller for smaller B . The ratio $n(\text{H}_2)/n(\text{H})$ depends exponentially on $(S_1 - S_2)/T = (Q_2 - Q_s)/T \simeq (Q_2 - Q_\infty)/T$. From Figure 1, we see that $Q_\infty - Q_2 > 0$ for $B_{12} \gtrsim 10$, and increases with increasing B . Therefore, when $B_{12} \gg 10$, there are few H_2 molecules compared with H atoms in the saturated vapor. The ionization ratio $n_p/n(\text{H})$ in the vapor depends exponentially on $(Q_s - Q_1)/(2T)$. From Figure 1, we see that $Q_\infty - Q_1 > 0$ when $B_{12} \gtrsim 200$, in which case the vapor mostly consists of ionized hydrogen (cf. Fig. 5(c)). For $10 \lesssim B_{12} \lesssim 200$, $n(\text{H})$ is greater than n_p and $n(\text{H}_2)$, although the abundances of larger molecules are also appreciable.

The column density y_{sat} above the surface of the condensed phase is related to the saturation vapor pressure P_{sat} by $y_{\text{sat}} = P_{\text{sat}}/g$ and is plotted against T in Figure 6 for $B_{12} = 10, 100, 500$ (all for $g_{14} = 1$). Note that T is the temperature at the gas/metal phase boundary. The density of the vapor is typically $\rho \sim m_p g y / (kT) \sim 10 g_{14} T_5^{-1} y$ (g cm^{-3}). Using equation (3.6) for the magnetic free-free opacity, we obtain the optical depth of the vapor above the metallic hydrogen, $\tau_{\text{ff}} \sim 400 \beta g_{14} T_5^{-5/2} B_{12}^{-2} y^2$. The threshold vapor column density y_{th} , below which the vapor is optically thin, is then given by

$$y_{\text{th}} \sim 0.05 \beta^{-1/2} g_{14}^{-1/2} B_{12} T_5^{5/4} \text{ (g cm}^{-3}\text{)}. \quad (4.10)$$

This threshold value y_{th} is also plotted against T in Fig. 6. The intersect of the $y_{\text{sat}}(T)$ and $y_{\text{th}}(T)$ curves defines a “threshold photospheric temperature” $T_{\text{ph,th}}$ for the optical depth above the surface of the condensate (if any): For $T_{\text{ph}} > T_{\text{ph,th}}$, the photosphere is purely in the gaseous phase, as described in §3. For $T_{\text{ph}} < T_{\text{ph,th}}$ the vapor above the condensed metal is optically thin, and there is a sharp change in density at the gas/metal interface; The “photosphere” is located inside the condensed phase. For $B_{12} = 500$, the saturated vapor is dominated by ionized hydrogen, hence the value for $T_{\text{ph,th}}$ should be fairly accurate. For $B_{12} = 10$ and 100, however, the vapor is dominated by atoms or molecules, free-free opacity is only an estimate and thus the values of $T_{\text{ph,th}}$ given in Fig. 6 are more approximate. In any case, we see that $T_{\text{ph,th}}$ is only slightly less than the condensation temperature T_{crit} .

In the case of $T_{\text{ph}} < T_{\text{ph,th}}$, the pressure at the gas/metal interface P_{sat} is less than P_{ph} . Some distance into the condensed phase, with pressure increasing from P_{sat} to P_{ph} (which is still much less than P_{crit} for the condensed phase), the liquid is still optically thin and T stays close to T_{ph} . Further still into the metal, as P increases toward P_{crit} from the “liquid photosphere”, the temperature increases appreciably while the density increases only slowly. Whether this region is convective or radiative depends on the opacity law in the condensed metal, which we have not yet investigated.

5. DISCUSSIONS

Recent works on the equation of state of neutron star surface in strong magnetic field have focused on the outer crust consisting of iron-like elements (e.g., Fushiki et al. 1989; Abrahams & Shapiro 1991). Heat transport through this crustal region can be affected by the strong magnetic field (e.g., Hernquist 1985). However, for a neutron star covered by hydrogen atmospheric layer, the outer crust of the solid lattice is not the directly observable region of the star. Recent theoretical modeling of neutron star atmosphere aims at interpreting ROSAT’s soft X-ray spectra from several radio pulsars, and most studies have focused on ionized atmospheres (Pavlov et al. 1995; Zavlin et al. 1995).

Our present study indicates that for sufficiently low temperature ($T \lesssim 10^6$ K) and/or high magnetic field ($B \gtrsim 10^{12}$ G), hydrogen atoms or molecules can have large abundance in the photosphere (see Fig. 2). This relatively large neutral abundance (even at relatively high temperature) comes about mainly for two reasons: (i) The binding energies of the bound states are greatly increased by the magnetic field; (ii) The photospheric density is much larger because the surface gravity is strong and also because the opacity of one of the two photon modes is significantly reduced by the magnetic field. Therefore one could in principle expect some atomic or molecular line features in the soft X-ray or UV spectra. In particular, the Lyman ionization edge (160 eV at 10^{12} G and 310 eV at 10^{13} G) is expected to be prominent by the following consideration: The free-free and bound-free cross-sections for a photon in the extraordinary mode (with the photon electric field perpendicular to the magnetic field) are approximately given by (Gnedin, Pavlov & Tsygan 1974; Ventura et al. 1992; Potekhin & Pavlov 1993):

$$\sigma_{\text{ff}\perp} \simeq 1.7 \times 10^3 \rho T_5^{-1/2} \alpha^2 a_o^2 \omega^{-1} b^{-2}, \quad \sigma_{\text{bf}\perp} \simeq 4\pi\alpha a_o^2 \left(\frac{Q_1}{\omega}\right)^{3/2} b^{-1},$$

where $\alpha = 1/137$ is the fine structure constant, a_o is the Bohr radius, ρ is the density in g cm^{-3} , ω is the photon energy in the atomic units, Q_1 is the ionization potential, and b is the dimensionless field strength defined in Eq. (1.1). Near the absorption edge, the ratio of the free-free and bound-free opacities is

$$\frac{\kappa_{\text{ff}\perp}}{\kappa_{\text{bf}\perp}} \sim 10^{-4} \frac{\rho}{T_5^{1/2} B_{12} X(\text{H})}.$$

Thus even for relatively small neutral H abundance $X(\text{H})$, the discontinuity of the total opacity at the Lyman edge is pronounced.⁶ Clearly, the position and the strength of the absorption edge can provide a useful diagnostic of the neutron star surfaces.

For even stronger magnetic field (B larger than a few times 10^{13} G), we have shown that the degenerate matter can extend all the way to the outer edge of the star with little gaseous atmosphere above it, if the effective surface temperature T_{eff} is less than a threshold value $T_{\text{ph,th}}$ (cf. Fig. 6). In this case, the thermal radiation arises from just below the metallic hydrogen surface. Using equation (3.1) as an estimate for the condensation density (near zero pressure), we find that the electron plasma frequency Ω_e is given by $\hbar\Omega_e \simeq 0.66 B_{12}^{3/5}$ keV, much larger than the typical photon energy $kT \simeq 10 T_5$ eV. Thus photons cannot be easily excited thermally inside the metallic surface. As a result, the surface emission is reduced from the black-body emission with the same temperature, and the spectrum of the surface radiation is likely to deviate quite strongly from a black-body spectrum (e.g., Itoh 1975; Brinkmann 1980). We have not investigated the opacity structure of the hydrogen condensate and cannot say whether the emission mimics highly diluted blackbody radiation with color temperature much larger than the effective surface temperature.

Finally, we note that the possibility that the outermost layer of a neutron star consists of degenerate iron has been considered previously, based on the notion that in a strong

⁶ Since the extraordinary mode has smaller opacity, most of the X-ray flux will come out in this mode. For photons in the ordinary mode, we have $\sigma_{\text{ff}\parallel} \simeq 1.65 \times 10^3 \rho T_5^{-1/2} \alpha^2 a_o^2 \omega^{-3}$ (the zero-field value), and $\sigma_{\text{bf}\parallel} \simeq 10^2 \pi \alpha a_o^2 (Q_1/\omega)^{5/2} (\ln b)^{-2}$, which give $\kappa_{\text{ff}\parallel}/\kappa_{\text{bf}\parallel} \sim 10^{-2} \rho T_5^{-1/2}$ for $B_{12} \sim 1$. Thus the absorption edge for the ordinary mode is less pronounced.

magnetic field the cohesive energy of Fe solid can be as large as tens of keV (Ruderman 1974). While it is certainly correct that a strong magnetic field can significantly enhance the cohesive energy, it has been shown (Neuhauser et al. 1987) that the earlier calculation (Flowers et al. 1977) greatly overestimated the cohesive energy of Fe solid (cf. §2.3.2). Thus the metallic iron surface scenario was replaced by a non-degenerate atmosphere model. Our results in this paper partially resurrects the “degenerate surface picture”: hydrogen (not iron) can condensate at sufficiently high B field and low temperature.

This work has been supported in part by NASA Grant NAGW-2394 and NAG 5-2756 to Caltech, and by NSF Grant AST 91-19475, NASA Grant NAGW-666 and NAG 5-3097 to Cornell University. D.L. also acknowledges the support of a Richard C. Tolman Research Fellowship in theoretical astrophysics at Caltech.

APPENDIX A. ESTIMATE THE RELATIVE BINDING ENERGY BETWEEN 1D CHAIN AND 3D CONDENSATE

In the absence of self-consistent electronic structure calculation for the 3d condensed metal, we estimate the fractional relative binding energy, $\Delta E_s/|E_\infty| = (E_s - E_\infty)/|E_\infty|$, using the following three methods:

(i) *Method 1*: If we approximate the 1d chain by an uniform cylinder (radius R , proton spacing a), then the energy per atom (subcylinder) in the chain can be written as

$$E_\infty = \frac{2\pi^2}{3b^2R^4a^2} - \frac{1}{a} \left[\ln \frac{2a}{R} - \left(\gamma - \frac{3}{4} \right) \right], \quad (\text{A1})$$

where $\gamma = 0.57721566$ (see Paper I). Minimizing E_∞ with respect to R and a gives

$$R = 1.694b^{-2/5}, \quad a/R = 1.885, \quad E_\infty = -0.3913b^{2/5}. \quad (\text{A2})$$

Comparing with equation (2.8) for the energy of 3d metal in the Wigner-Seitz approximation, we find $\Delta E_s/|E_\infty| \simeq -1\%$.

(ii) *Method 2*: Imagine that the 3d condensate is formed by placing a pile of parallel chains in contact with each other. The chain is assumed to have the property given by equation (A2). For a body-centered tetragonal lattice, the relative position of nearest neighboring protons is $x_0 = 2R$ perpendicular to the field and $z_0 = a/2$ parallel to the field. We calculate the electrostatic interaction energy E_{12} between a pair of nearest neighboring subcylinders using a Monte-Carlo integration method (Interaction between subcylinders of larger separations can be calculated using a quadrupole-quadrupole formula, but this interaction is small compared to the nearest neighbor interaction). This gives $E_{12} = -3.7 \times 10^{-4}b^{2/5}$. Since each proton has eight nearest neighbors, we have $\Delta E_s = 4E_{12}$, and thus $\Delta E_s/|E_\infty| \simeq -0.4\%$.

If we choose $x_0 < 2R$ (which would involve overlap of electron clouds), the chain-chain interaction is stronger. For $x_0 = \sqrt{2}R$ (the smallest value possible), we find $\Delta E_s/|E_\infty| \simeq -8\%$. We consider this as an upper limit to the true relative binding energy.

(ii) *Method 3*: Similar to (ii), we form 3d solid by placing chains together into a body-centered tetragonal lattice, with $x_0 = 2R$ and $z_0 = a/2$. But instead of equation (A2), we determine R and a by minimizing the total energy of the solid, $E_s = E_\infty + \Delta E_s$, where E_∞

is given by equation (A1), and the numerical result for $\Delta E_s = 4E_{12}$ can be fitted by the following analytic formula (with accuracy $\lesssim 1\%$ for $1.6 \leq a/R \leq 2.2$):

$$\Delta E_s = -4.0 \times 10^{-4} \frac{1}{R} \left[1 + 23 \left(\frac{a}{R} - 1.4 \right)^2 \right]. \quad (\text{A3})$$

Minimizing $E_s(R, a)$, we obtain:

$$R = 1.650 b^{-2/5}, \quad a/R = 2.036, \quad E_s = -0.3932 b^{2/5}. \quad (\text{A4})$$

Comparing with equation (A2) for a single chain, we find $\Delta E_s/|E_\infty| \simeq -0.5\%$.

APPENDIX B. PYCNUCLEAR REACTIONS INDUCED BY STRONG MAGNETIC FIELD

In this appendix, we consider the interesting possibility of ‘‘cold fusion’’ of hydrogen bound states induced by strong magnetic field on the neutron star surfaces. The magnetized H molecules and condensed metal are highly compressed, i.e., the internal electron density within these bound states is large. This results in strong screening to the ion-ion Coulomb potential, and, as we will show, dramatic increase in the fusion rate between the nuclei within the bound states.

Nuclear reaction in bound molecular systems has been studied in the context of muon-catalysed fusion, where a massive muon replaces the electron in a diatomic molecule of hydrogen isotope, enhancing the binding and producing large cold fusion rates (e.g., Zel’dovich & Gershtein 1961). In astrophysics, nuclear reactions induced by high matter density (‘pynuclear reactions’) have also been studied (e.g., Salpeter & Van Horn 1969; Schramm & Koonin 1990). The magnetic field induced fusion is similar to the density-induced pynuclear reaction except that the large density increase comes from the formation of bound states in strong magnetic field.

We consider the enhancement of the fusion rate by magnetic field in both molecules and condensed metals.

B.1 Internal Fusion of H₂

Consider a diatomic molecule composed of two isotopic nuclei of hydrogen. The fusion rate Λ is proportional to the probability density $|\Psi(r_n)|^2$ that the two nuclei are at contact, i.e., $\Lambda = A|\Psi(r_n)|^2$, where A is the nuclear reaction constant which is directly related to the astrophysical S factor, and r_n is the nuclear radius. The relative wavefunction Ψ of the two nuclei is governed by the interatomic potential $V(r)$, which has been calculated in Paper I and II in the strong magnetic field regime. We can write $V(r)$ in the form:

$$V(r) = \frac{1}{r} - \frac{1}{r_0} + E(\text{H}_2) - \Delta V(r), \quad (\text{B1})$$

where r_0 is the equilibrium separation, $E(\text{H}_2)$ is the equilibrium energy of the molecule, and the function $\Delta V(r) = 0$ at $r = r_0$ and increases to $[E(\text{H}_2) - 1/r_0 - E(\text{He})]$ as r decreases to zero ($E(\text{He})$ is the ground-state energy of He atom). For the molecule in the ground state, the relative energy E_r of the two nuclei is simply $E(\text{H}_2)$ plus the zero-point energy $\hbar\omega_{\parallel}/2$

(we consider vibration along the field axis only). In the WKB approximation, $|\Psi(r_n)|^2$ is proportional to the WKB penetration factor P , i.e.,

$$|\Psi(r_n)|^2 \propto P = \exp(-W), \quad W = 2\sqrt{2\mu} \int_{r_n}^{r_c} [V(r) - E_r]^{1/2} dr, \quad (B2)$$

where r_c is the classical inner turning point, μ is the reduced mass of the two nuclei in units of the electron mass.

Neglecting $\Delta V(r)$, equation (B2) can be easily integrated to give $W \simeq \pi(2\mu r_c)^{1/2}$, with $r_c = (1/r_0 + \hbar\omega_{\parallel}/2)^{-1}$. A fitting formula for the numerical values of r_0 given in Paper I and Paper II is $r_0 \simeq 12.7(\ln b)^{-2.2}$. With $r_c \simeq r_0$ we have $W \simeq 15.8\sqrt{\mu}(\ln b)^{-1.1}$. The numerical results calculated using the exact potential $V(r)$ and zero-point energy (see Eq. [2.4]) are given in Table 2, where the values of $\lambda = W/\sqrt{\mu}$ for different field strength are listed (λ does not depend sensitively on μ ; e.g., for $B_{12} = 1$, $\lambda \simeq 1.74$ for pp molecule and $\lambda \simeq 1.75$ for dd molecule.) These numerical results can be fitted by

$$W = 15.3\sqrt{\mu} (\ln b)^{-1.2}, \quad (B3)$$

which is reasonably close to the approximate analytic expression. The factor λ and the fusion rates for zero-field molecules as calculated by Koonin & Nauenberg (1989) are also listed in Table 2 for comparison. The reactions considered are: $p+p \rightarrow {}^2\text{H} + e^+ + \nu_e$, $p+d \rightarrow {}^3\text{He} + \gamma$, $p+t \rightarrow {}^4\text{He} + \gamma$, $d+d \rightarrow {}^3\text{He} + n \oplus {}^3\text{H} + p$, $d+t \rightarrow {}^4\text{He} + n$. Rescale the zero-field fusion rates using the appropriate λ for strong field, we immediately infer the fusion rates for molecules in strong magnetic field.⁷ These are listed in Table 2. Clearly, the strong magnetic field increases the fusion rate by many orders of magnitude. The energy generation rate per gram of molecules is $\sim 10^{18} \text{A erg g}^{-1} \text{s}^{-1}$.

B.2 Internal Fusion of H_N Chains

Larger H_N molecules (before saturation; see §2.2) have similar electronic potential and excitation energies as H_2 . Therefore similar enhancement to the fusion rates also occurs in H_N molecules, and this enhancement becomes more pronounced as N (and the field strength) increases. For a long chain molecule H_N with $1 \ll N \ll N_s \sim [b/(\ln b)^2]^{1/5}$, the spacing r_0 along a field line between adjacent protons decreases with increasing N approximately as⁸ $r_0 \sim 1/(N^2 \ln b)$ (Paper I), and thus $W \sim r_0^{1/2} \sim 1/N$. A deviation δr from the equilibrium spacing would give an excess potential $\delta V \sim (\ln b)(\delta r)^2/r_0^3$. Thus the fractional zero-point vibration amplitude $\Delta r/r_0$ is of order $(m_e/m_p)^{1/4} N^{1/2}$, i.e., the aligned vibrations become more pronounced as N increases. Both the decrease in r_0 and the increase in $\Delta r/r_0$ tend to enhance the nuclear reaction rate.

B.3 Fusion in Metallic Hydrogen

As mentioned in §2.3, the zero-pressure metallic hydrogen has nonuniform electron distribution. Although this screening effect will certainly increase the fusion rate, the essential

⁷ In the strong magnetic field, the wavefunction Ψ for the two nuclei is not spherical, unlike the field-free case. Therefore the proportional factor in $\Lambda \propto \exp(-\lambda\sqrt{\mu})$ is different for $B = 0$ and for high field cases, and our values for the fusion rate at high B are not exact. However, since the dominant factor determining the fusion rate is still the penetration factor, the error should not exceed an order of magnitude.

⁸ Note that this is the asymptotic limiting result. For small N , the scaling with b is closer to $r_0 \sim (\ln b)^{-2}$.

TABLE 2
Bound state fusion rates for isotopic hydrogen molecules

	Reactions ^a	pp	pd	pt	dd	dt
	μ/m_p	1/2	2/3	3/4	1	6/5
B_{12}	$\log_{10} A$ (cm ³ s ⁻¹)	-39.1	-21.3	-20.3	-15.8	-13.9
	λ ^b	$\log_{10} \Lambda$ s ⁻¹				
0	4.13	-64.4	-55.0	-57.8	-63.5	-68.9
1	1.74	-32.9	-18.7	-19.3	-19.0	-20.2
5	1.35	-27.8	-12.7	-13.0	-11.8	-12.2
10	1.22	-26.1	-10.8	-10.9	-9.3	-9.6
100	.895	-21.8	-5.8	-5.7	-3.3	-3.0
500	.740	-19.8	-3.5	-3.2	-0.4	0.2

^a The reactions are given in the text.

^b λ is defined via $P = \exp(-\lambda\sqrt{\mu})$; and the values are given for the pd system; see text.

feature can be obtained in the uniform electron gas model. As an estimate, we can simply use the fitting formula of Salpeter and van Horn (1969; see also Schramm & Koonin 1990) for the pycnonuclear reaction rate, except that the zero-pressure density is given by equation (3.1). For pd reaction, the rate per deuteron is $\Lambda_{\text{pd}} \simeq 2 \times 10^{13} \rho_6^{7/12} \exp(-21.8 \rho_6^{-1/6})$ s⁻¹. Thus a deuteron embedded in a cold hydrogen plasma has lifetime $\Lambda_{\text{pd}}^{-1} = 10^{9.6}$ years at $B_{12} = 2$ and one year at $B_{12} = 13$. For pp fusion, the reaction rate is $\Lambda_{\text{pp}} \simeq 800 \rho_6^{7/12} \exp(-18.89 \rho_6^{-1/6})$ yr⁻¹. At $B_{12} = 60, 100, 500$, corresponding to zero-pressure densities $\rho_{s,0} \simeq 7.6 \times 10^4, 1.4 \times 10^5, 10^6$ g cm⁻³, we find $\Lambda_{\text{pp}}^{-1} \simeq 10^{10.3}, 10^9, 10^{5.3}$ yrs, respectively. Thus for non-accreting neutron star, there is an upper limit to the field strength above which the surface hydrogen layer is absent. Comparing with Table 2, we see that at a given field strength, the fusion rate is larger in the metallic state than in molecule. The reason is that the mean ion separation in the condensed state decreases with increasing field strength as a power-law function of B , whereas the mean interatomic separation in a molecule decreases only logarithmically. Also note that as the matter density or temperature increase, the magnetic field effects become less important because many Landau levels are occupied by the electrons.

REFERENCES

- Abrahams, A. M., & Shapiro, S. L. 1991, *ApJ*, 374, 652
- Ashcroft, N. W., & Mermin, N. D. 1976, *Solid State Physics* (Saunders College: Philadelphia), p.337
- Avron, J. E., Herbst, I. B., & Simon, B. 1978, *Ann. Phys. (NY)*, 114, 431
- Becker, W. 1995, *Ann. N.Y. Acad. Sci.*, 759, 250
- Blaes, O., & Madau, P. 1993, *ApJ*, 403, 690
- Brinkmann, W. 1980, *A&A*, 82, 352
- Callaway, J., & March, N. H. 1984, *Solid State Phys.*, 38, 135
- Canuto, V., Lodenguai, J., & Ruderman, M. 1971, *Phys. Rev.*, D3, 2303
- Ceperley, D., & Alder, B. 1980, *Phys. Rev. Lett.*, 45, 566
- Chiu, H. Y., & Salpeter, E. E. 1964, *Phys. Rev. Lett.*, 12, 413
- Duncan, R. C., & Thompson, C. 1992, *ApJ*, 392, L9
- Edelstein, J., & Bowyer, S. 1996, in *Pulsars: Problems and Progress*, Ed. S. Johnston, M. A. Walker & M. Bailes (ASP Conference Series, Vol. 105), p291.
- Flowers, E. G., et al. 1977, *ApJ*, 215, 291
- Fushiki, I., Gudmundsson, E. H., & Pethick, C. J. 1989, *ApJ*, 342, 958
- Fushiki, I., Gudmundsson, E. H., Pethick, C. J., & Yngvason, J. 1992, *Ann. Phys. (NY)*, 216, 29
- Gnedin, Yu. N., Pavlov, G. G., & Tsygan, A. I. 1974, *Sov. Phys. JETP*, 39, 201
- Hansen, J. P., & Pollock, E. L. 1973, *Phys. Rev. A*, 8, 3110
- Hernquist, L. 1985, *MNRAS*, 213, 313
- Herold, H., Ruder, H., & Wunner, J. 1981, *J. Phys. B: At. Mol. Phys.*, 14, 751
- Horing, N. J. 1969, *Ann. Phys. (NY)*, 54, 405
- Itoh, N. 1975, *MNRAS*, 173, 1P
- Jones, P.B. 1985, *MNRAS*, 216, 503
- . 1986, *MNRAS*, 218, 477
- Kadomtsev, B.B. 1970 *Sov. Phys. JETP*, 31, 945
- Khersonskii, V. K. 1987, *Sov. Astron.*, 31, 225
- Koonin, S. E., & Nauenberg, M. 1989, *Nature*, 339, 691
- Lai, D., Salpeter, E. E., & Shapiro, S. L. 1992, *Phys. Rev. A*, 45, 4832 (Paper I)
- Lai, D., & Salpeter, E. E. 1996, *Phys. Rev. A*, 53, 152. (Paper II)
- . 1995, *Phys. Rev. A*, 52, 2611 (Paper III)
- Landau, L. D., & Lifshitz, E. M. 1980, *Statistical Physics, Part 1*, 3rd Ed. (Pergamon: Oxford)
- Lieb, E. H., Solovej, J. P., & Yngvason, J. 1994, *Commun. Math. Phys.*, 161, 77
- Lodenguai, J., Canuto, V., Ruderman, M., & Tsuruta, S. 1974, *ApJ*, 190, 141
- Miller, M.C. 1992, *MNRAS*, 255, 129
- Nelson, R. W., Salpeter, E. E., & Wasserman, I. 1993, *ApJ*, 418, 874
- Neuhauser, D., Koonin, S. E., & Langanke, K. 1987, *Phys. Rev. A*, 36, 4163
- Paczynski, B. 1992, *Acta Astron.*, 42, 145
- Pavlov, G. G., Shibano, Y. A., Ventura, J., & Zavlin, V. E. 1994, *A&A*, 289, 837
- Pavlov, G. G., Shibano, Y. A., Zavlin, V. E., & Meyer, R. D. 1995, in “Lives of Neutron Stars”, eds. A. Alpar, U. Kiziloglu & J. van Paradijs (Kluwer: Dordrecht)
- Pavlov, G. G., Zavlin, V. E., Trümper, J., & Neuhäuser, R. 1996, *ApJ*, 472, L33
- Pethick, C. J. 1992, *Rev. Mod. Phys.*, 64, 1133
- Potekhin, A. Y. 1994, *J. Phys. B.*, 27, 1073

- Potekhin, A. Y., & Pavlov, G. G. 1993, ApJ, 407, 330
Rajagopal, M., & Romani, R. W. 1996, ApJ, 461, 327
Reisenegger, A. 1995, ApJ, 442, 749
Romani, R. W. 1987, ApJ, 313, 718
Ruder, H. et al. 1994, Atoms in Strong Magnetic Fields (Springer-Verlag)
Ruderman, M. 1971, Phys. Rev. Lett., 27, 1306
———. 1974, in “Physics of Dense Matter” (I.A.U. Symp. No. 53), ed. C.J. Hansen
(Dordrecht-Holland: Boston), p.117
Salpeter, E. E., & van Horn, H. M. 1969, ApJ, 155, 183
Schramm, S., & Koonin, S. E. 1990, ApJ, 365, 296
Shemi, A. 1995, MNRAS, 275, L7
Silant’ev, N. A., & Yakovlev, D. G. 1980, Ap. Space Sci., 71, 45
Thompson, C., & Duncan, R. C. 1993, ApJ, 408, 194
Treves, A., & Colpi, M. 1991, A&A, 241, 107
Tsuruta, S. 1964, Ph.D. thesis, Columbia University
Umeda, H., Tsuruta, S., & Nomoto, K. 1994, ApJ, 433, 256
Ventura, J., Herold, H., Ruder, H., & Geyer, F. 1992, A&A, 261, 235
Walter, F. M., Wolk, S. J., & Neuhäuser, R. 1996, Nature, 379, 233
Zel’dovich, Ya. B., & Gershtein, S. S. 1961, Sov. Phys. Uspekhi, 3, 593
Zavlin, V. E. et al. 1995, A&A, 297, 441
Zavlin, V. E., Pavlov, G. G., & Shibbanov, Y. A. 1996, A&A, 315, 141

FIGURE CAPTIONS

FIG. 1.— Energy releases from several atomic and molecular processes as a function of the magnetic field strength. The solid line shows the ionization energy Q_1 of H atom, the dotted line shows the dissociation energy Q_2 of H_2 , and the dashed line shows the cohesive energy Q_∞ of linear chain H_∞ . The zero-point energy corrections have been included in Q_2 and Q_∞ .

FIG. 2.— Temperature-density diagram of the atmosphere of a neutron star with surface field strength (a) $B_{12} = 1$ and (b) $B_{12} = 10$, both with $g_{14} = 1$. The solid lines correspond to the photosphere (“ $\tau \simeq 2/3$ ”) and the extraordinary photon emission region (“ $\tau_\perp \simeq 2/3$ ”); the dotted curves (“e+p=H”) correspond to constant neutral H fractions, with $n(H)/n_g = 0.9$ for the lower curves, $n(H)/n_g = 0.5$ (half/half ionization) for the middle curves, and $n(H)/n_g = 0.1$ for the upper curves; the dashed curves (“H+H= H_2 ”) correspond to the half/half dissociation of H_2 ; the long-dashed lines (“ $T = T_F$ ”) show the Fermi temperature; the dot-long-dashed lines show selected temperature-density profiles of atmospheres with different photospheric temperatures ($T_{\text{ph},5} = 5, 2$ for $B_{12} = 1$ and $T_{\text{ph},5} = 9, 3$ for $B_{12} = 10$); the dot-dashed vertical lines (“ $\rho = \rho_{\text{Landau}}$ ”) correspond to the density above which the electrons occupy the excited Landau level; the dark vertical lines correspond to the condensation density $\rho_{s,0}$; The filled circles correspond to the photospheric “ionization temperature” $T_{\text{ph,ir}}$ (see text).

FIG. 3.— Neutral fraction $n(H)/n_g$ as a function of temperature at a fixed density $\rho = n_g m_p = 0.01 \text{ g/cm}^3$ (heavy lines) and 0.1 g/cm^3 (light lines). The curves are labeled by the field strength: $B_{12} = 0.01$ (solid lines), 0.1 (short-dashed lines), 1 (long-dashed lines), 10 (dot-dashed lines). The zero-field results are also shown for comparison (dotted lines).

FIG. 4.— Abundance of various H species as a function of the photosphere temperature at a point with $P = P_{\text{ph}}/2$ (just a little above the photosphere) for three field strengths (a) $B_{12} = 1$, (b) 10 , and (c) 100 . The fractional number density are defined by $X(H_N) = n(H_N)/n_{\text{tot}}$, $X_p = n_p/n_{\text{tot}}$, with $n_{\text{tot}} = 2n_p + n(H) + n(H_2) + \dots$. The numbers labeling each curve specify N , with, e.g., “3-5” indicating $X(H_3) + X(H_4) + X(H_5)$.

FIG. 5.— The saturation vapor densities of various species (in the atomic units, a_0^{-3}) of condensed metallic hydrogen as a function of temperature for different magnetic field strengths: (a) $B_{12} = 10$; (b) $B_{12} = 100$; (c) $B_{12} = 500$. The dotted curves give n_p , the short-dashed curves give $n(H)$, the long-dashed curves give $n(H_2)$, the dot-dashed curves give $[3n(H_3) + 4n(H_4) + \dots + 8n(H_8)]$, and the solid curves give the total baryon number density in the vapor $n_g = n_p + n(H) + 2n(H_2) + \dots$. The horizontal solid lines denote the condensation density $n_s \simeq 50 B_{12}^{6/5}$ (a.u.), while the vertical solid lines correspond to the critical condensation temperature at which $n_g = n_s$.

FIG. 6.— Column density of saturated vapor. The heavy (steeper) lines show the column density y of the nondegenerate gas above the condensed metallic phase as a function of the temperature at the phase boundary, the lighter lines show the threshold column densities y_{th} (Eq. [4.10]) below which the vapor is optically thin to free-free absorption. The solid lines are for $B_{12} = 10$, the short-dashed lines for $B_{12} = 100$, and the long-dashed lines for $B_{12} = 500$, all with $g_{14} = 1$. The filled circles and vertical dotted lines correspond to the threshold photospheric temperature $T_{\text{ph,th}}$ below which the saturated vapor is optically thin.

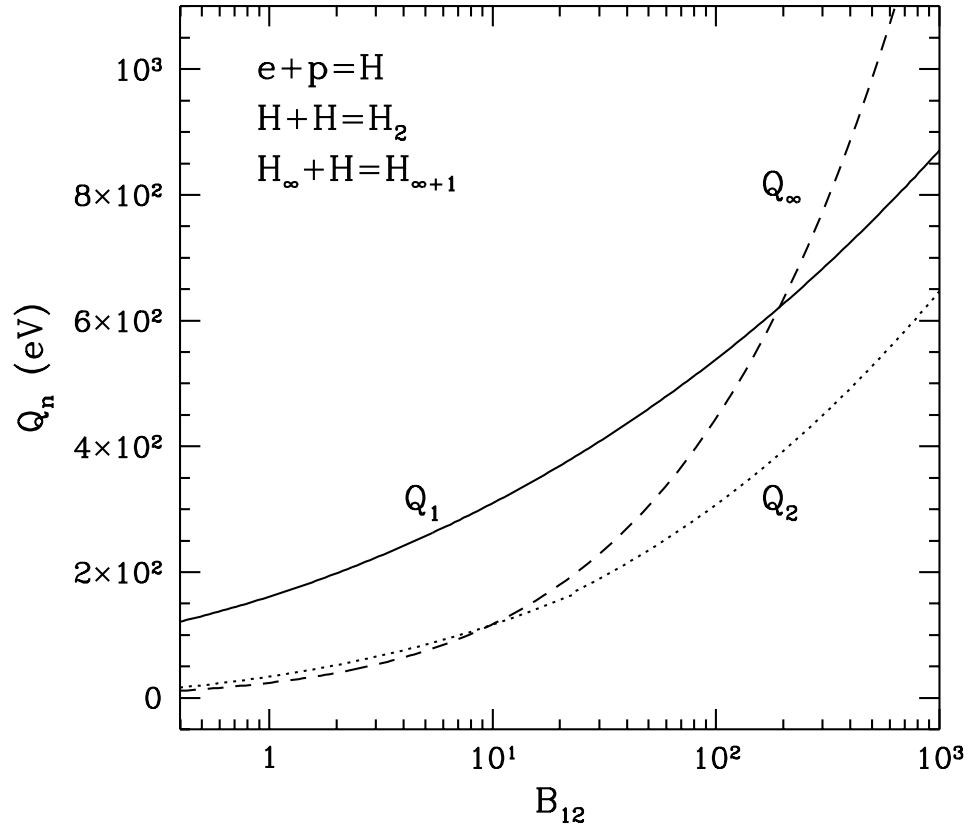


Fig. 1.—

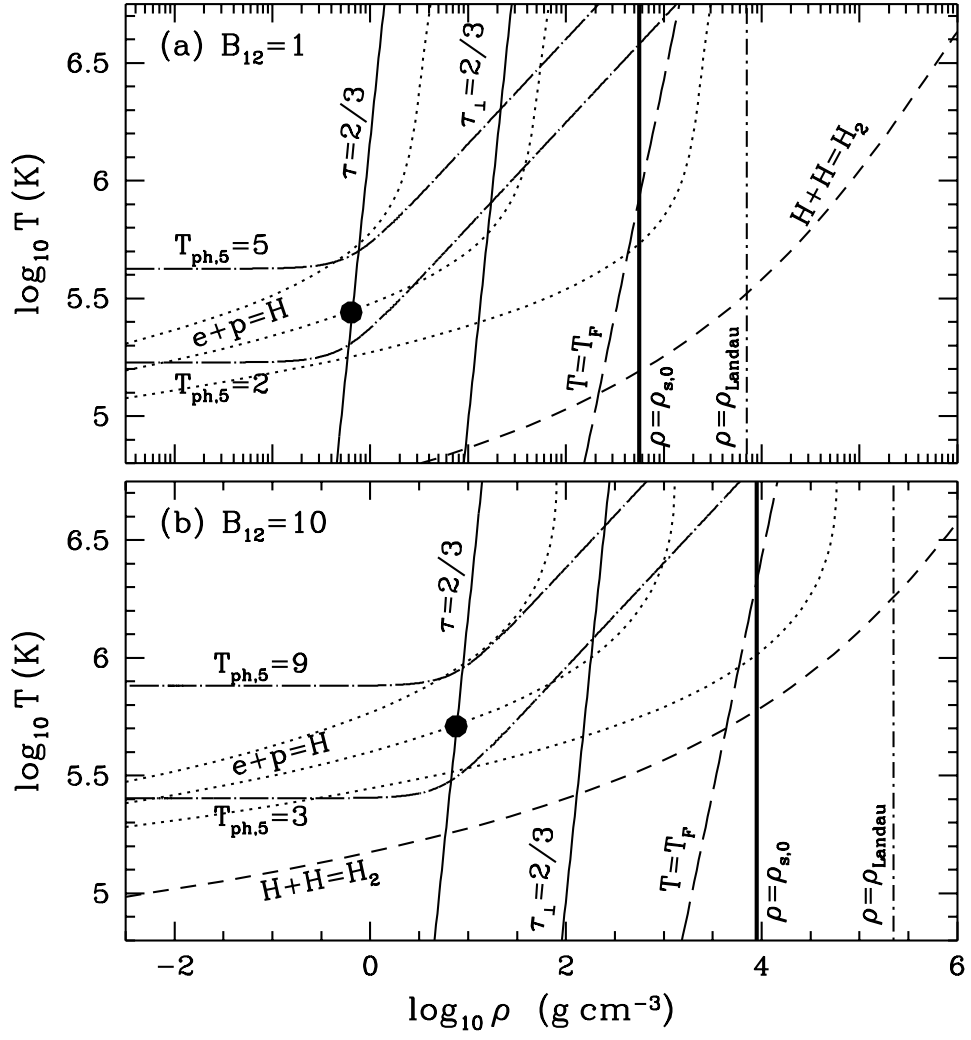


Fig. 2.—

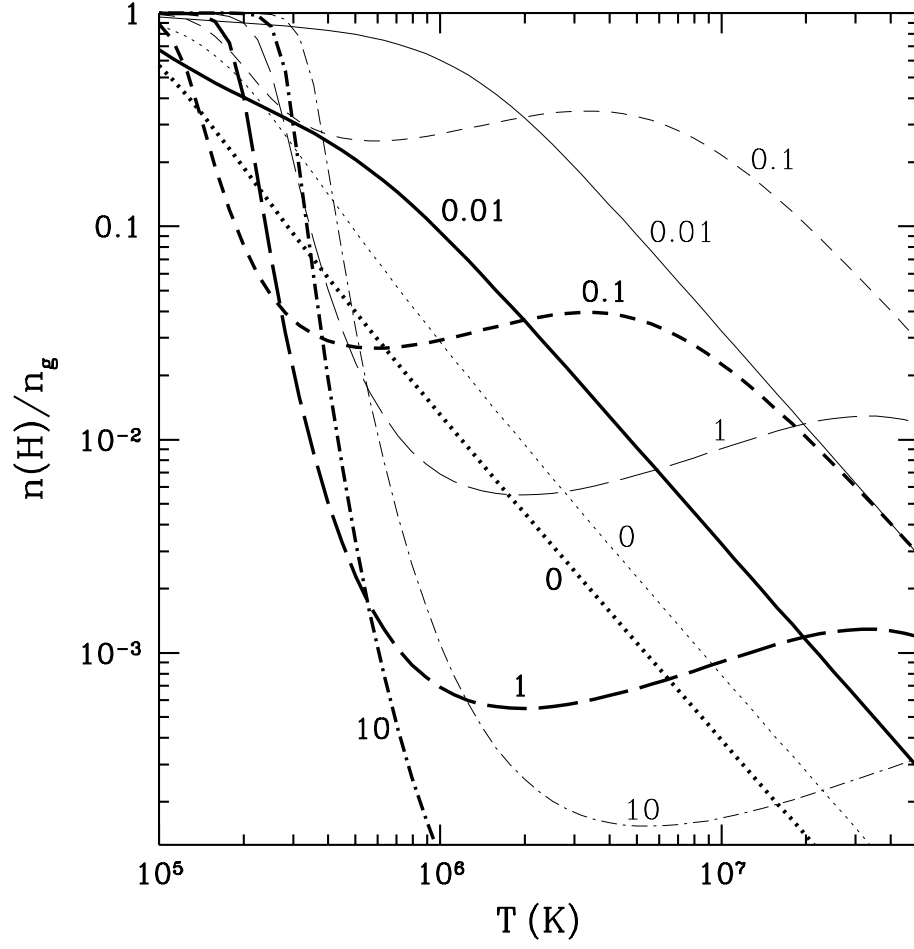


Fig. 3.—

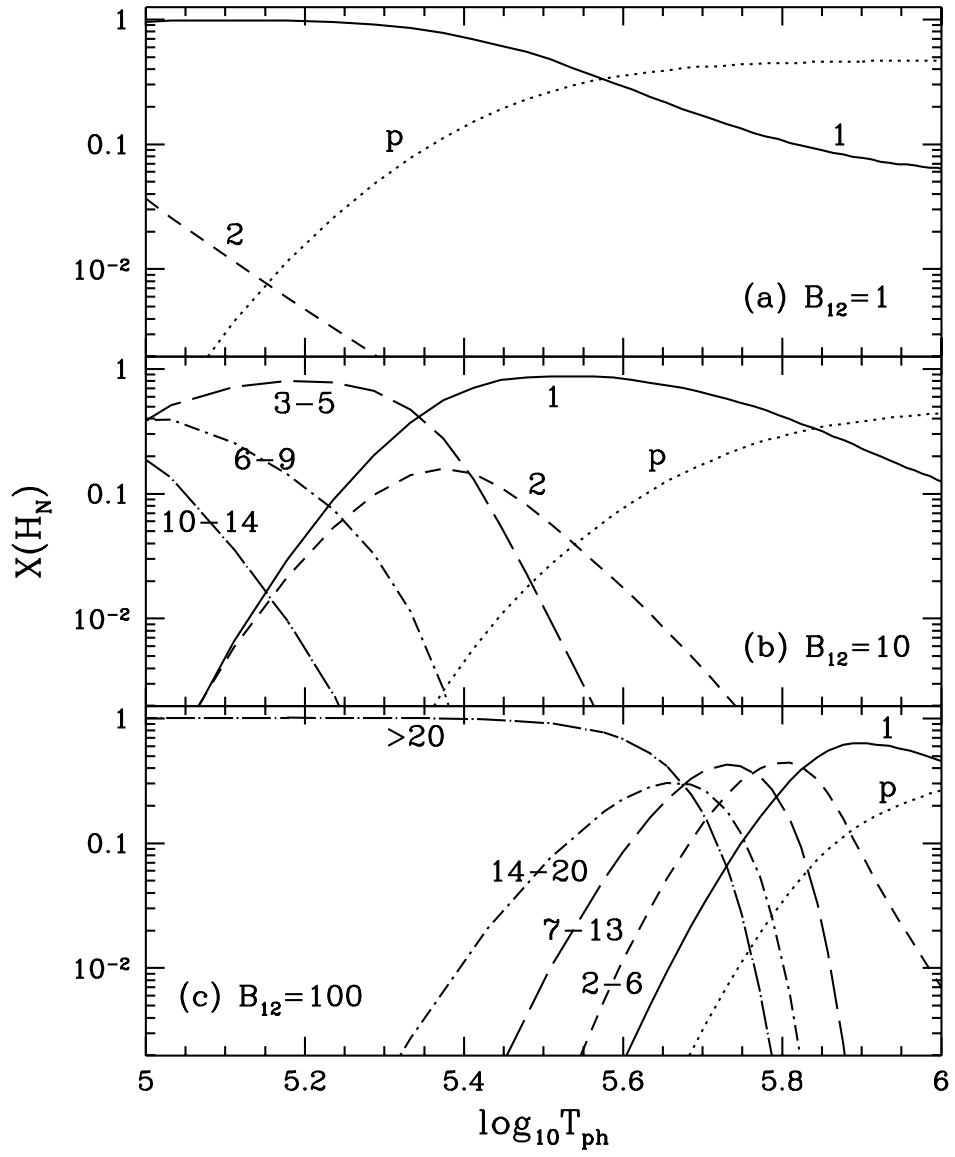


Fig. 4.—

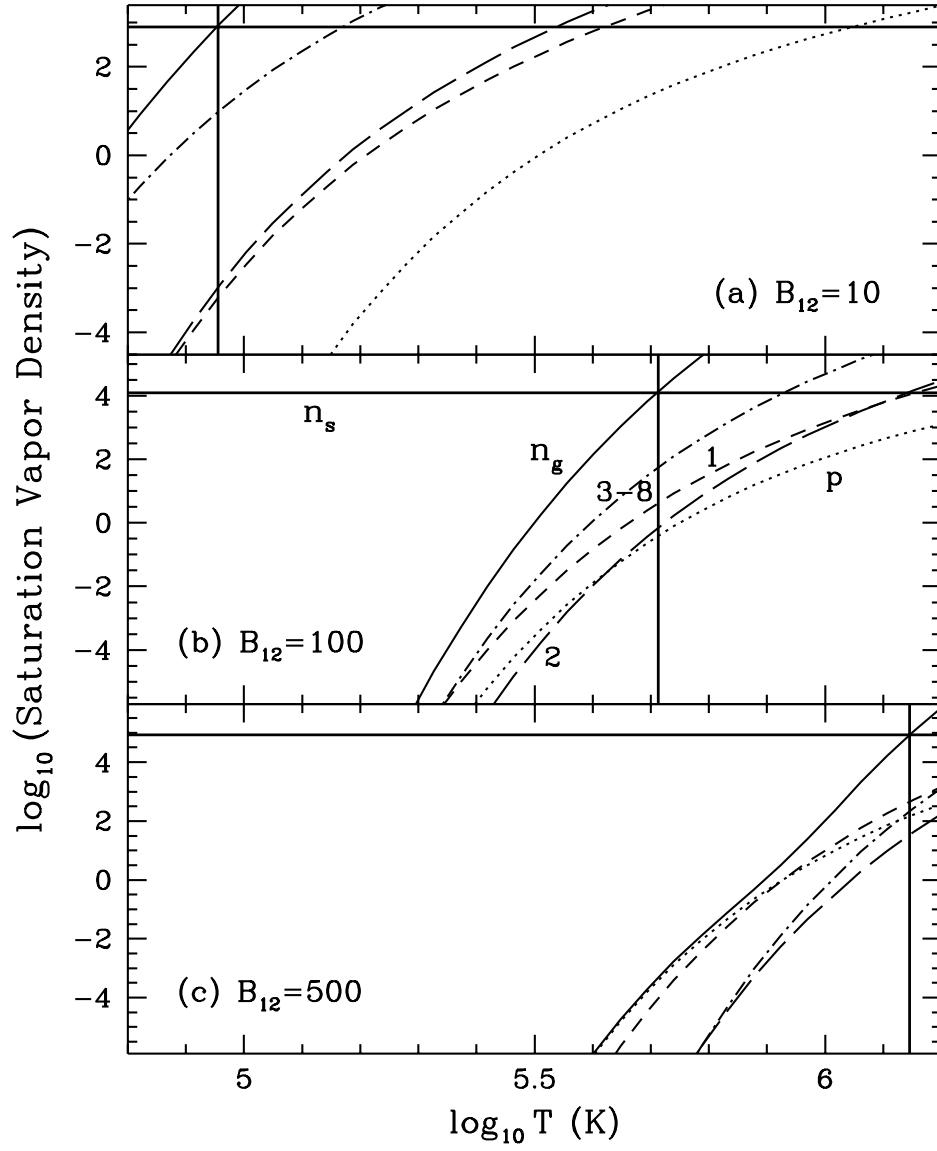


Fig. 5.—

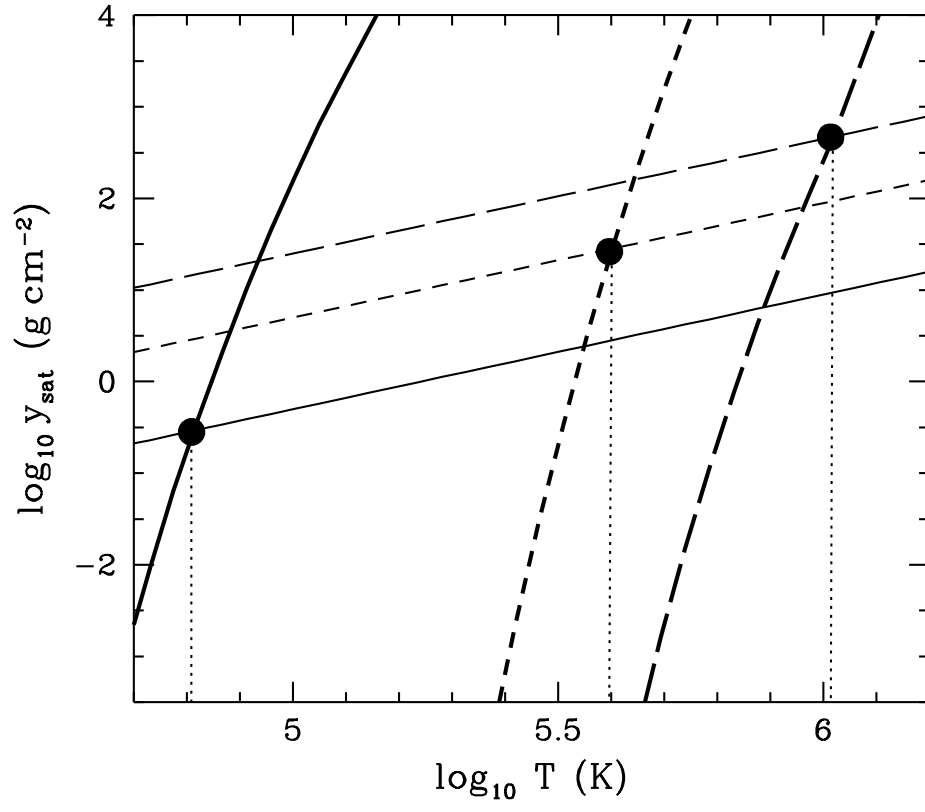


Fig. 6.—